Materials Science & Engineering A 796 (2020) 139977

Contents lists available at ScienceDirect

Materials Science & Engineering A

journal homepage: http://www.elsevier.com/locate/msea

Low-density, W-free Co–Nb–V–Al-based superalloys with γ/γ' microstructure

Fernando L. Reyes Tirado, Spencer V. Taylor, David C. Dunand [*,1]

Department of Materials Science and Engineering, Northwestern University, 2220 Campus Dr., Evanston, IL, 60208, USA

ARTICLE INFO

Keywords:
Cobalt-base superalloys
Atom probe tomography (APT)
Microstructure
Creep
Precipitates

ABSTRACT

Previously-reported metastable γ'-L1$_2$ $Co_3(Nb_{0.65}V_{0.35})$ precipitates in the Co–6Nb–6V (at. %) ternary alloy are stabilized by additions of Al, Ti, Ni and Cr to the alloy. We identify two such multinary γ/γ' alloys - with compositions of Co–10Ni–6Ti–5Al-xCr-3Nb–3V-0.04B at.% (with x = 0 and 4% Cr) - with γ'-precipitates remaining stable for up to 1000 h at 850 °C, with no additional phases present. Decreasing the Ti concentration from 6 to 2%, two more γ/γ' superalloys - Co–10Ni–5Al-xCr-3Nb–3V–2Ti-0.04B (with x = 4 and 8% Cr) – are created with stable γ'-precipitates (measured for 168 h at 850 °C) with morphologies more cuboidal than for the first two alloys with 6%Ti. These submicron cuboidal γ' precipitates are arranged into crystallographically-oriented sheets with small (<50 nm) γ'-spacing within sheets and larger (~100 nm) γ'-spacing between sheets. The alloy with the highest 8% Cr concentration shows, after aging at 850 °C for 24 h, γ'-nanoprecipitates with $(Co_{0.85}Ni_{0.15})_3(Ti_{0.13}Al_{0.25}\ Nb_{0.24}Cr_{0.21}V_{0.16}B_{0.01})$ composition (assuming full segregation onto the two sublattices), with Al and Ti replacing at a similar rate both Nb and V in the ternary $Co_3(Nb_{0.65}V_{0.35})$. This high-Cr alloy exhibits the best oxidation resistance, as seen by a reduction in the parabolic growth rate constant and surface oxide thickness. Also, the present W- and Ta-free, Cr-containing superalloys show good creep resistance at 850 °C, which is comparable to other recent Cr-containing Co-base γ/γ' superalloys with higher densities: (i) W-containing Co–9W–9Al–8Cr (at.%), and (ii) Ta-containing Co–10Ni–5Al–4Cr–3Ta–3V–2Ti-0.04B (at.%). This is the first report of a family of Co–Nb–V–Al-based γ/γ'-superalloys with low density (<8.0 g/cm^3).

1. Introduction

Nickel-based superalloys are currently the preferred materials for turbine blades used in high temperature applications such as jet engines and land-based power generation [1–4]. This is because of their high temperature stability and mechanical properties which stem from their γ+γ' microstructure [1]. Many researchers have recently studied Co-based superalloys following the 2006, report [5] that ternary Co–Al–W alloys exhibit L1$_2$-ordered γ'-precipitates in a disordered fcc γ-matrix, in agreement with a doctoral thesis published in 1971 [6]. Cobalt-based superalloys are an attractive option to replace Ni-based superalloys given the higher melting point of Co (1495 vs. 1455 °C in Ni), which could allow higher operation temperatures. Co–Al–W-based alloys display high solidus and liquidus temperatures as compared to Ni-based alloys [7,8], but they suffer from lower solvus temperature [5, 8–13], inferior long-term γ'-stability [9,10,12,13] and high density (due to the very high W content, ~25 wt%) [7,9,10].

To address the high-density issue in Co–Al–W-based superalloys, researchers have replaced W with combinations of elements such as Ta, Ti, Nb, Mo, Cr, and V [7,9,10,14–29]. The first family of W-free Co-based superalloys with a γ+γ'-microstructure was introduced by Makineni et al. [14–17] and is based on Co–10Al–5Mo-2X (X = Nb and Ta) quaternary alloys. This was followed by many investigations given the potential to surpass the density-corrected mechanical properties exhibited by Co–Al–W superalloys [27,28,30–32]. However, the γ'-phase was found to be metastable after long aging times at 800–900 °C in many of these alloys, with the exception of Co–30Ni–10Al–5Mo–2Nb–2Ti [10, 15,17].

In recent years, many other ternary systems have been identified to exhibit precipitation of stable L1$_2$ γ'-precipitates, e.g. Co-Ti-Cr [18,19], Co-Ti-Mo [19], Co–Ti–V [20,21] and Co–Al–V [22]. Recently, we reported the presence γ'-precipitates in Co–Ta–V and Co–Nb–V ternary alloys, after aging for short times at 900 °C, which however decomposed to the C36 phase in the Co–Ta–V system and to the D0$_{19}$ phase in the

* Corresponding author.
E-mail addresses: f.reyes@u.northwestern.edu (F.L. Reyes Tirado), spencervt97@gmail.com (S.V. Taylor), dunand@northwestern.edu (D.C. Dunand).
[1] Currently at: Department of Materials Science and Nano-engineering, Rice University, 6100 Main Street MS 325, Houston, TX, 77005, USA.

https://doi.org/10.1016/j.msea.2020.139977
Received 17 April 2020; Received in revised form 17 July 2020; Accepted 20 July 2020
Available online 3 August 2020

Co–Nb–V system at longer aging times [9]. In ternary Co–Ta–V alloys, we showed that metastable γ′- $L1_2$ $Co_3(Ta_{0..76}V_{0.24})$ phase was be stabilized by additions of Al and Ti as partial replacement of Ta and V [10]. Further improvements were achieved by adding Ni, Ti and Cr to create multinary Co–10Ni–5Al–3V–3Ta–2Ti-0.04B-xCr (x = 0 and 4) W-free alloys whose γ′-phase was stable up to 1000 h at 850 °C, with good creep resistance [10]. Chen et al. [22] showed improvements in Co–Al–V-based alloys using the same set of elements, which led to an alloy of similar composition (Co–30Ni–10Al–5V–4Ta–2Ti) with good coarsening resistance and high γ′- solvus temperature [22], albeit, with higher amount of Ni and γ′-formers (Al, V, Ta and Ti) and without Cr which is needed for oxidation resistance [1].

Here, we take a similar approach as with Co–Ta–V-based alloys [10] to stabilize the metastable γ′-phase in Co–6Nb–6V [9] and we create Co–6Nb–6V [9]low-density alloys that exhibit good coarsening-, creep- and oxidation resistance. As done with the Co–Ta–V system [10], the new alloying elements which we select for these Co–6Nb–6V-based alloys are: (i) Al and Ti, which help stabilized the γ′-phase in Co–Ta–V-based alloys and are known to partition to the γ′-phase in Co-based superalloys [10,33–37]; (ii) Ni, which expands the γ+γ′ phase field in Co-based superalloys [38–40]; (iii) Cr, which improves oxidation and corrosion resistance [1,41–43]; and (iv) B, which provides solid-solution strengthening and inhibits grain-boundary sliding during creep [12,44,45]. Thus, our hypothesis is that the light elements Al, Ti, Cr and B - which were successfully used to stabilize the metastable γ′-phase in Co–6Ta–6V [9] - have the same effect in Co–6Nb–6V, thus demonstrating a new family of Co-based γ/γ′ superalloys achieving low densities by avoiding the use of Mo, W and Ta. In the following, we show that the γ′-phase in these Co–Nb–V-based compositions is indeed stabilized for a range of alloys containing most of these elements after aging at 850 °C. An optimized alloy with composition Co–10Ni–8Cr–5Al–3Nb–3V–2Ti-0.04B (at.%) shows good creep resistance at 850 °C (compared to Co–Ta–V-based alloys and Cr-containing Co–Al–W alloys), high hardness and oxidation resistance, while maintaining a low density (due to lack of dense W and Ta).

2. Experimental procedures

Ingots with nominal compositions of Co–6Al–3Nb–3V, Co–5Al–3Nb–3V–1Ti, Co–10Ni–6Ti–5Al-xCr-3V–3Nb-0.04B (x = 0 and 4) and Co–10Ni-xCr-5Al–3Nb–3V–2Ti-0.04B (x = 4 and 8) were arc-melted using high-purity Co (99.9+%), Ni (99.98%), Cr (99.99%), Al (99.99%), Nb (99.95%), V (99.7%), Ti (99.95%) and B (99.95%). These six multinary alloys are listed in Table 1, together with our prior ternary alloy (Co–6Nb–6V) which exhibited a metastable γ/γ′ microstructure [9]. Also reported in Table 1 are nine ternary Co–Nb–V alloys studied by Wang et al. [46] during their experimental investigation of the Co–Nb–V phase diagram, with higher Nb content (5–25 at.%) and/or V content (10–35 at.%) than our alloys; none of their arc-melted ternary alloys showed the γ/γ' microstructure after aging at 1000 °C (for 1080 h) or 1200 °C (for 600 h) and water-quenching.

Our ingots, with a mass of ~10–20 g, were arc-melted a minimum of five times under a partial Ar atmosphere and flipped between each melt cycle to improve homogeneity. The arc-melted ingots were then vacuum-encapsulated in quartz ampoules and homogenized at 1200 °C for 48 h, followed by water quenching. Specimens sectioned from the ingot were vacuum-encapsulated in quartz ampoules for aging heat-treatments. The Co–6Al–3Nb–3V and Co–5Al–3Nb–3V–1Ti alloys were aged at 850 °C for 168 h (1 week), the Co–10Ni–6Ti–5Al-xCr-3V–3Nb-0.04B (x = 0 and 4), Co–10Ni–5Al–4Cr–3Nb–3V–2Ti-0.04B and Co–10Ni–8Cr–5Al–3Nb–3V–2Ti-0.04B alloys were aged at 850 °C for 24, 72, 168, 500 and 1000 h (~7 weeks). All alloys were water-quenched following the aging heat treatment.

Polished cross-sections were imaged via scanning electron microscopy (SEM) using a FEI Quanta 650 SEM, equipped with an Oxford Aztec silicon drift detector (SDD) energy dispersive spectrometer (EDS).

Table 1
Nominal composition of Co–Nb–V-based alloys (at.%) from prior studies and the present work.

Alloy	Co	Ni	Cr	Nb	V	Al	Ti	B	γ-γ′ structure
Prior studies									
Wang et al. [42]	85	–	–	10	5	–	–	–	no
	75	–	–	20	5	–	–	–	no
	75	–	–	15	10	–	–	–	no
	75	–	–	10	15	–	–	–	no
	70	–	–	10	20	–	–	–	no
	65	–	–	25	10	–	–	–	no
	65	–	–	5	30	–	–	–	no
	60	–	–	10	30	–	–	–	no
	60	–	–	5	35	–	–	–	no
Reyes Tirado et al. [9]	88	–	–	6	6	–	–	–	metastable
Present study									
1	88	–	–	3	3	6	–	–	no
2	88	–	–	3	3	5	1	–	no
3 (6Ti–0Cr)	73	10	–	3	3	5	6	0.04	yes
4 (6Ti–4Cr)	69	10	4	3	3	5	6	0.04	yes
5 (2Ti–4Cr)	73	10	4	3	3	5	2	0.04	yes
6 (2Ti–8Cr)	69	10	8	3	3	5	2	0.04	yes

All specimens were ground using 320, 400, 600, 800, 1200 grit SiC paper, polished using 6, 3, and 1 μm diamond suspension, and chemically etched at room temperature using Carapella's reagent.

Vickers microhardness was measured at ambient temperature on polished cross-sections of the Co–10Ni–6Ti–5Al-xCr-3V–3Nb-0.04B (x = 0 and 4) and Co–10Ni–8Cr–5Al–3Nb–3V–2Ti-0.04B alloys at an applied load of 3 N for a 5s dwell time. Each hardness value is the average of 20 measurements performed over multiple grains. High-temperature compression creep tests were performed on the Co–10Ni–6Ti–5Al-xCr-3V–3Nb-0.04B (x = 0) and Co–10Ni-xCr-5Al–3Nb–3V–2Ti-0.04B (x = 4 and 8) alloys in air at 850 °C for a range of increasing stresses, using a dead-load creep frame. Creep samples were machined in the form of cylinders (6 mm in height and 3 mm in diameter) by wire electro-discharge machining (EDM) and aged for 168 h at 850 °C, followed by water quenching. Creep specimens were water-quenched immediately after unloading, followed by sectioning in parallel and perpendicular directions to the applied load. The same SEM sample preparation and imaging techniques were used to characterize the crept specimens.

Composition analysis and partitioning coefficients for the γ- and γ' phases were determined by Atom Probe Tomography (APT) for Co–10Ni–6Ti–5Al-xCr-3V–3Nb-0.04B (x = 0 and 4) and Co–10Ni–8Cr–5Al–3Nb–3V–2Ti-0.04B homogenized alloys aged for 24 h at 850 °C. Nanotip specimens were prepared via a focused-ion beam (FIB) lift-out technique using a Ga + dual-beam in a FEI Helios Nanolab SEM/FIB instrument. Rectangle-topped wedges were attached to a Si micropost on a coupon and sharpened using Ga^+ to a 20–50 nm minimum tip radius. APT was performed using a Cameca local-electrode atom-probe (LEAP) 5000X–Si system with a picosecond ultraviolet (wavelength = 355 nm) laser, a specimen temperature of ~25 K, a pulse energy of 25 pJ, a 500-kHz pulse repetition rate and a 4–8% detection rate.

Differential Scanning Calorimetry (DSC) was performed on Co–10Ni–6Ti–5Al-xCr-3V–3Nb-0.04B (x = 0 and 4% Cr) and Co–10Ni-xCr-5Al–3Nb–3V–2Ti-0.04B alloys using a Netzsch STA 449 F3 Jupiter instrument to determine γ′ solvus temperature. Before DSC measurements, homogenized samples were aged for 24 h at 850 °C followed by water quenching, and then segmented into 20–50 mg pieces. During DSC experiments, the samples were heated from 25 to 1200 °C (at 20 °C/min) under an Ar atmosphere and held for 1 h at 1200 °C to allow dissolution of the γ' phase. Cooling was performed from 1200 to 25 °C (at the same rate of 20 °C/min) followed by a 10-min hold at 25 °C. This cycle was repeated three times.

Thermal Gravimetric Analysis (TGA) was performed on Co–10Ni–6Ti–5Al-xCr-3V–3Nb-0.04B (x = 0 and 4) and Co–10Ni–8Cr–5Al–3Nb–3V–2Ti-0.04B alloys using a Mettler Toledo TGA/SDTA85 instrument to determine the isothermal oxidation resistance of the alloys. Before TGA experiments, homogenized samples were aged at 850 °C for 24 h followed by water quenching, and then machined into rectangular specimens (4.45 × 3.48 × 1.83 mm). These specimens were placed in an alumina crucible (4 mm in diameter and 3 mm in height) for the test. Isothermal experiments were performed at 850 °C for 20 h with dry air supplied at 50 mL/min, and at a heating/cooling rate of 10 °C/min. Specimens from the TGA experiments were mounted in cold-setting epoxy right after TGA isothermal oxidation tests. The oxide scale thickness of the outermost oxide layer was measured using ImageJ and represents an average of 60 measurements over 5 images per sample.

3. Results and discussion

3.1. Microstructure evolution

3.1.1. Effect of Al and Ti additions on γ' phase stability

In our previous study of ternary Co–Nb–V alloys [9], we reported γ′-precipitation in an alloy with nominal composition Co–6Nb–6V after homogenization at 1200 °C for 48 h and subsequent furnace cooling. These metastable γ′-precipitates, with $Co_3(Nb_{0.65}V_{0.35})$ composition as determined via APT, were consumed by $D0_{19}$ needle-like precipitates after only 16 h of aging at 900 °C. Experiments where these ternary Co–6Nb–6V specimens were homogenized and water-quenched, followed by aging at 900 °C (terminated by water quenching), did not yield γ′-precipitation; instead, $D0_{19}$ needle-like precipitates with a Co_3X composition were observed [9]. A similar behavior was seen in ternary Co–6Ta–6V specimens, where γ′-precipitates formed after aging at 900 °C and were consumed by the discontinuous precipitation of a Ta-rich C36 phases at longer aging times [9,10]. We then showed that the γ′-precipitates in the Co–Ta–V system are stabilized by the addition of Al and Ti [10], which are known to be γ′-formers and, in the case of Al, needed for oxidation resistance. These alloying additions, where half (3 at.%) of the Ta and V concentrations were replaced with 3 at.% of Al and Ti, produced γ+γ′ microstructures that were found to be stable after up to 168 h of aging at 850 and 900 °C [10].

Here, a similar approach is followed to stabilize the γ′-phase in the Co–6Nb–6V system: half the Nb and V (3 at.% each) content are replaced with Al (required for oxidation resistance), for a cumulative amount of 6 at.%, which produces the first alloy studied here: Co–6Al–3Nb–3V. Furthermore, Ti additions in Co-based superalloys are known to stabilize the γ′-phase, increase the solvus temperature of the γ′-phase [8,17,47,48] and increase the strength of the alloys [37], given that Co–12Ti shows precipitation of the γ′-phase [10,18,19,21,37,49–51]. Hence, for our second alloy, 1 at. % Al in the first, quaternary Co–6Al–3Nb–3V alloy is replaced by 1 at. % Ti, leading to the second, quinary alloy, Co–5Al–3Nb–3V–1Ti. Fig. 1 shows these two alloys after homogenization at 1200° for 48 h and aging at 850 °C for 168 h, followed by water quenching. For Co–6Al–3Nb–3V, a single γ-phase is achieved within grains while eutectic-like regions are present at the grain boundaries after homogenization. Aging for 168 h at 850 °C leads to precipitation of $D0_{19}$ needle-like precipitates like those seen in Co–6Nb–6V [9]. Replacing 1 at.% Al for 1 at.% Ti also produces a single-phase γ microstructure with eutectic-like regions at the grain boundaries in the

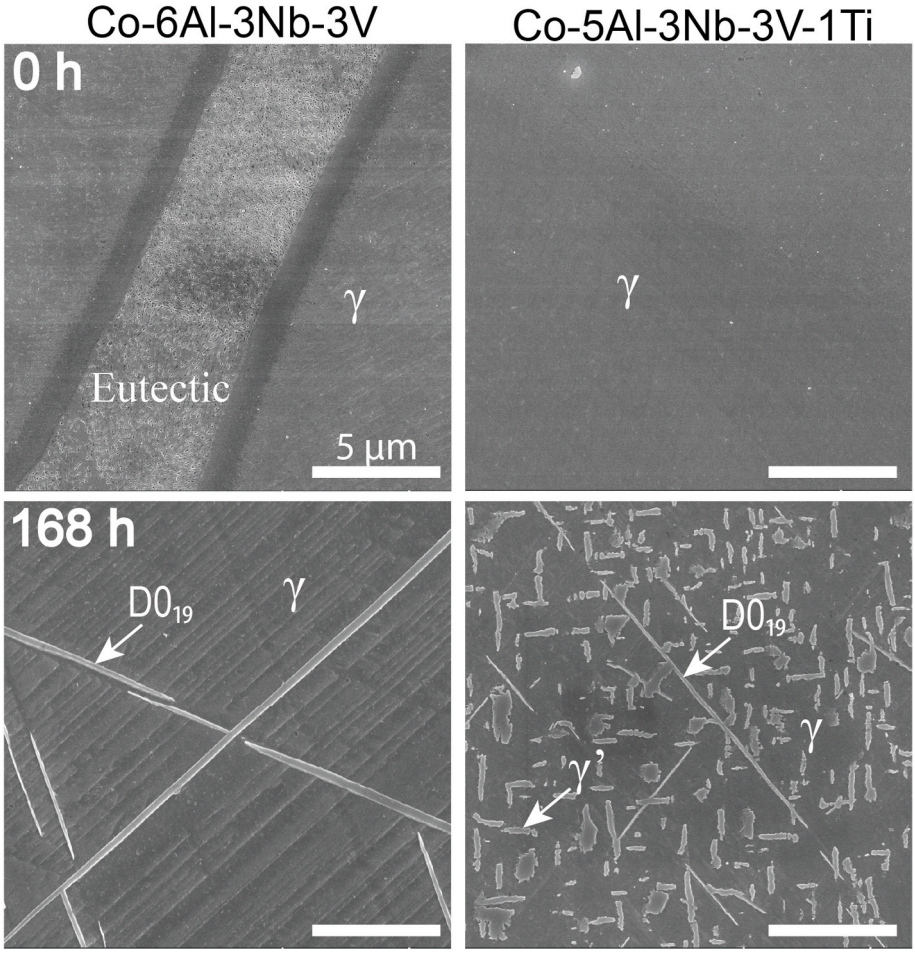

Fig. 1. SEM micrographs of Co–6Al–3Nb–3V and Co–5Al–3Nb–3V–1Ti aged at 850 °C for 168 h. The γ-matrix is deep-etched to show the γ′ and $D0_{19}$ phases.

as homogenized state. After aging for 168 h at 850 °C followed by water quenching, both γ′-precipitates and $D0_{19}$ needle-like precipitates are present in the microstructure. Low magnification images of the microstructure can be found in Fig. S1 of Supplementary Information.

Thus, Ti and Al additions to the present Co–Nb–V-based alloy stabilizes the γ′-phase, as also observed in previously studied Co–Ta–V-based alloys [10]. However, unlike the prior Co–Ta–V-based alloys, Al alone does not serve as a stabilizing agent, making Ti a required alloying element to produce a stable γ′-phase. This is consistent with the fact that the Co–Ti binary system is the only binary system where γ′-precipitation is observed, in alloys with a Co–12Ti [10,18,19,21,37,49–53] composition, where the γ′-phase has a high lattice misfit, leading to elongated coalesced precipitates [18,19]. Therefore, to stabilize the γ′-phase in the Co–12Ti system, many alloys have been investigated, where some of the Ti is being replaced or complemented by elements such as Cr [18,19], Mo [19], W [51] and V [21,50], which are reported to decrease the lattice misfit as compared to the binary Co–12Ti. This suggests that increasing the amount of Ti in our alloys will lead to a two-phase γ+γ′ microstructure, and that alloying with Cr will also lead to improvements in microstructure, as seen in Co–Ta–V-based alloys [10]. This approach is discussed in the following section.

3.1.2. *Multicomponent alloys with varying Cr additions*

In our prior study of Co–Ta–V-based alloys, we report the stabilization of the γ′-phase via Al, Ti and Cr additions, leading to the compositions Co–10Ni–5Al–3Ta–3V–2Ti-0.04B-xCr (x = 0 and 4) [10]. These alloys show cuboidal γ′-precipitates embedded in a γ-matrix that are stable up to 1000 h of aging at 850 °C with no other undesirable phases, and with grain boundaries decorated with γ′-precipitates [10]. Therefore, to stabilize the γ′-phase present in the second alloy presented here (Co–5Al–3Nb–3V–1Ti), a similar approach is followed, which leads to the four additional alloys studied here: Co–10Ni–6Ti–5Al-xCr-3V–3Nb-0.04B (x = 0 and 4, as third and fourth alloys) and Co–10Ni-xCr-5Al–3Nb–3V–2Ti-0.04B (x = 4 and 8, as fifth and sixth alloys). Similar to Co–10Ni–5Al–3Ta–3V–2Ti-0.04B-xCr (x = 0 and 4) [10], nickel (10 at. %) is added to increase the γ+γ′ phase-field, titanium is increased (from 1 to 6 at.%) in order to stabilized and increase the solvus temperature of the γ′-phase, boron (0.04 at.%) is added to inhibit grain boundary sliding, and chromium is added for oxidation and corrosion resistance. Given that, in the previous Co–Ta–V alloys, the addition of 4 at.% Cr does not produce undesirable phases [10] (such as $D0_{19}$ or μ (D_{85}) in Co–7Al–7W-(10, 13)Cr and Co–7Al–7W-(21,17)Cr, respectively [10,54]), the Cr amount is increased here from 0 to 4 at. % for alloys 4–6.

Fig. 2 shows the microstructural evolution of the third and fourth high-Ti alloys - Co–10Ni–6Ti–5Al-xCr-3V–3Nb-0.04B (x = 0 and 4) - aged at 850 °C for 24, 72, 168, 500 and 1000 h, referred to as 6Ti–0Cr and 6Ti–4Cr from here on. For both alloys, up to the longest aging time, grains display no other phases than crystallographically-aligned γ′-precipitates, and grain boundaries are decorated exclusively with coarsened γ′-precipitates (shown in Fig. S2). Such grain-boundary γ′-precipitates have also been reported in Co–Ta–V-based alloys (Co-(5–6)Al–3Ta–3V-(0–1)Ti and Co–10Ni–5Al–3Ta–3V–2Ti-0.04B-(0–4)Cr alloys) [10]. As illustrated in Fig. 2, the 6Ti–0Cr alloy exhibits small cuboidal γ′-precipitates within grains after 24 and 72 h of aging at 850 °C, with no other phases present. These precipitates coarsen and coalesce into sheets after 168 h of aging which do not seem to evolve much up to 1000 h of aging at 850 °C. In the 6Ti–4Cr alloy, the γ′-precipitates are cuboidal after 24 and 72 h of aging, and the volume fraction seems to increase slightly. After 168 h, the precipitates remain cuboidal, however, some regions show directional coarsening in sheets while others show coarsening and coalescence (Fig. S3). After 500 h, the γ′-precipitates coarsen and coalesce, forming irregular plate-like precipitates like those seen in the 6Ti–0Cr alloys, which do not seem to change significantly after 1000 h of aging. These irregular γ′-precipitates are similar to those seen in (i) Co–12Ti, when some of the Ti is replaced by Al and W, aged at 900 °C for 1000 h [37], and (ii) Co–11Ti–10Cr and Co–11Ti–15Cr [18] aged at 900 °C for 100 and 500 h. A high lattice misfit is identified as the cause for the elongated shape and irregular morphology of the γ′-precipitates, which later coalesce to a plate-like morphology [18,37]. A similar behavior was reported in Co–12Ti-(0

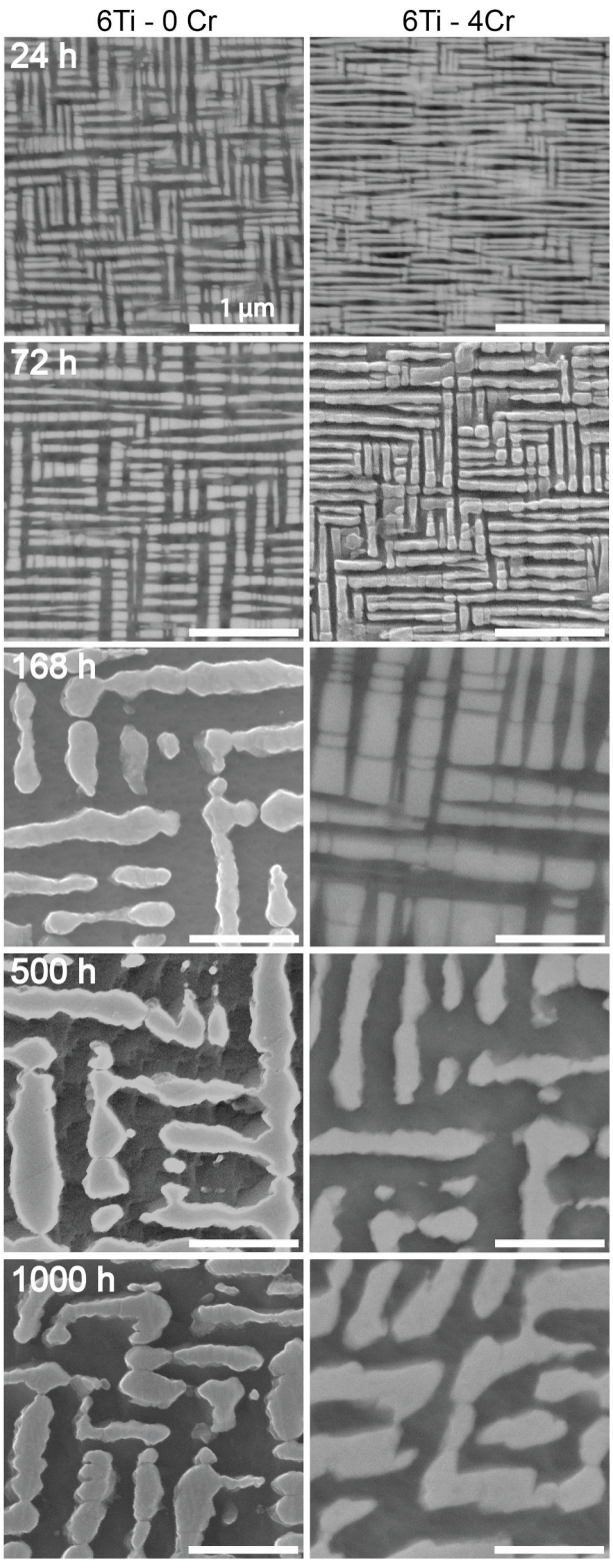

Fig. 2. SEM micrographs of Co–10Ni–6Ti–5Al-xCr-3Nb–3V-0.04B (x = 0 and 4, labeled 6Ti–0Cr and 6Ti–4Cr, respectively) aged at 850 °C for 24, 72, 168, 500 and 1000 h, showing γ/γ′ microstructure.

and 4)X (X = Mo or Cr), where elongated irregular γ′-precipitates arranged into plates are more noticeable in Co–12Ti than in Co–12Ti–4Mo or Co–12Ti–4Mo aged at 800 °C for 24 h, with Co–12Ti being the alloy with the highest lattice misfit [19]. Furthermore, Bocchini et al. reported analogous γ′-microstructures in Co–Ni–Al–W–Ti alloys with the same amount of Ti (6 at.%) and decreasing amounts of W [8], aged for 256 h at 900 and 1000 °C. Hence, the coarsening and coalescence into precipitates with irregular plate-like morphologies seen in our alloys, Fig. 2, is most probably due to high average misfit which might be mitigated by decreasing the Ti amount in the alloys.

We test this hypothesis in the fifth alloy, where the Ti content is decreased from 6 to 2 at. % Ti as compared to 6Ti–4Cr, resulting in a Co–10Ni–5Al–4Cr–3Nb–3V–2Ti-0.04B alloy (labeled as 2Ti–4Cr). The Cr content is doubled (from 4 to 8 at. %) in the sixth alloy to increase oxidation resistance, leading to a Co–10Ni–8Cr–5Al–3Nb–3V–2Ti-0.04B composition (referred to as 2Ti–8Cr). Fig. 3 shows the microstructural evolution for these 2Ti–4Cr and 2Ti–8Cr alloys, homogenized for 48 h at 1200 °C and aged at 850 °C for 24, 72, 168, 500 and 1000 h. In the 2Ti–4Cr alloy (left column of Fig. 3), cuboidal submicron γ′-precipitates are seen at early aging times (24, 72, and 168 h) in a directional plate-like arrangement, with ~100–200 nm γ′ inter-precipitate spacing between plates and <50 nm γ′ inter-precipitate spacing. The high-Cr alloy (2Ti–8Cr, right column of Fig. 3) shows a similar microstructure. For 2Ti–8Cr, some partial directional coarsening and coalescences is seen up to 1000 h at 850 °C, but γ′-precipitates maintaining their cuboidal shape up to 1000 h of aging much more than the high-Ti alloys, Fig. 2. The grain boundaries in these low-Ti alloys are also decorated by coarsened γ′-precipitates and are devoid of other precipitates (Fig. S4). The coarsening of precipitates was studied, for aging times between 24 and 1000 h at 850 °C, by measuring their area A from micrographs, from which a mean circular equivalent radius was calculated as: $<R(t)> = (A(t)/\pi)^{1/2}$. Fig. S5 shows the precipitate radius evolution for the 6Ti–0Cr, 6Ti–4Cr, 2Ti–4Cr and 2Ti–8Cr alloys; the data are fitted to a common coarsening law:

$$<R(t)> = <R_o(t) + Kt^{1/p} \quad (1)$$

where t represents the aging time, $R_o(t)$ the precipitate radius at the onset of coarsening, K the coarsening rate constant and p the temporal exponent. Quasi-steady-stationary coarsening predicts $1/p = 1/3$ based on the Lifshitz-Slyozov-Wagner (LSW) binary alloy model, Kuehman-Voorhees (KV) ternary alloy model [55], and the Philippe-Voorhees (PV) multicomponent alloy model [56]. For the high Ti alloys (6Ti–0Cr and 6Ti–4Cr), the temporal exponent values, 1/p, are 0.44 and 0.55 respectively, which indicates that the precipitates have not reached a quasi-steady-stationary state or that the precipitate evolution does not follow the above models, possibly due to the simultaneous coarsening and coalescence into elongated precipitates occurring in these alloys. For the low Ti alloys (2Ti–4Cr and 2Ti–8Cr), the temporal exponent values, 1/p, are 0.32 and 0.33 respectively, in good agreement with typical values ($1/p = 0.33$) for coarsening in the above LSW, KV and PV models. This is consistent with the cuboidal morphology of the precipitates being retained throughout coarsening.

The microstructure of 2Ti-(4 and 8)Cr (Fig. 3) is similar to that of 6Ti-(0 and 4)Cr (Fig. 2) at the early aging times (24 and 72 h): cuboidal precipitates are arranged into plates and coarsening and coalescence starts to occur in regions where large precipitates grow at the expense of the smaller ones. When comparing the 2Ti–4Cr and 6Ti–4Cr alloys (Figs. 2 and 3), it is apparent that increasing Ti leads to a slight increase in γ′-area fraction; however, the precipitates seem to coalesce and arrange into plates earlier in the 6Ti–4Cr alloy. In 6Ti–4Cr, a long arrangement of small cuboidal coalesced precipitates is seen after 24 h, which leads to the formation of plate-like precipitates; by contrast, in 2Ti–4Cr, the precipitates are arranged into plates but little coalescence is seen before 168 h. Hence, decreasing the Ti content of these alloys leads to higher stability (reduced coalescence) of the γ′-microstructure in these alloys after 168–1000 h of aging at 850 °C, most probably due to a decrease in lattice misfit. Such plate like arrangement during stress-free aging, like rafting during creep, has previously been reported in Co–30Ni–10Al–5Mo–3Nb–3Ti aged at 950 °C for 100 h and was again attributed to a high misfit between the γ- and γ′ phases.

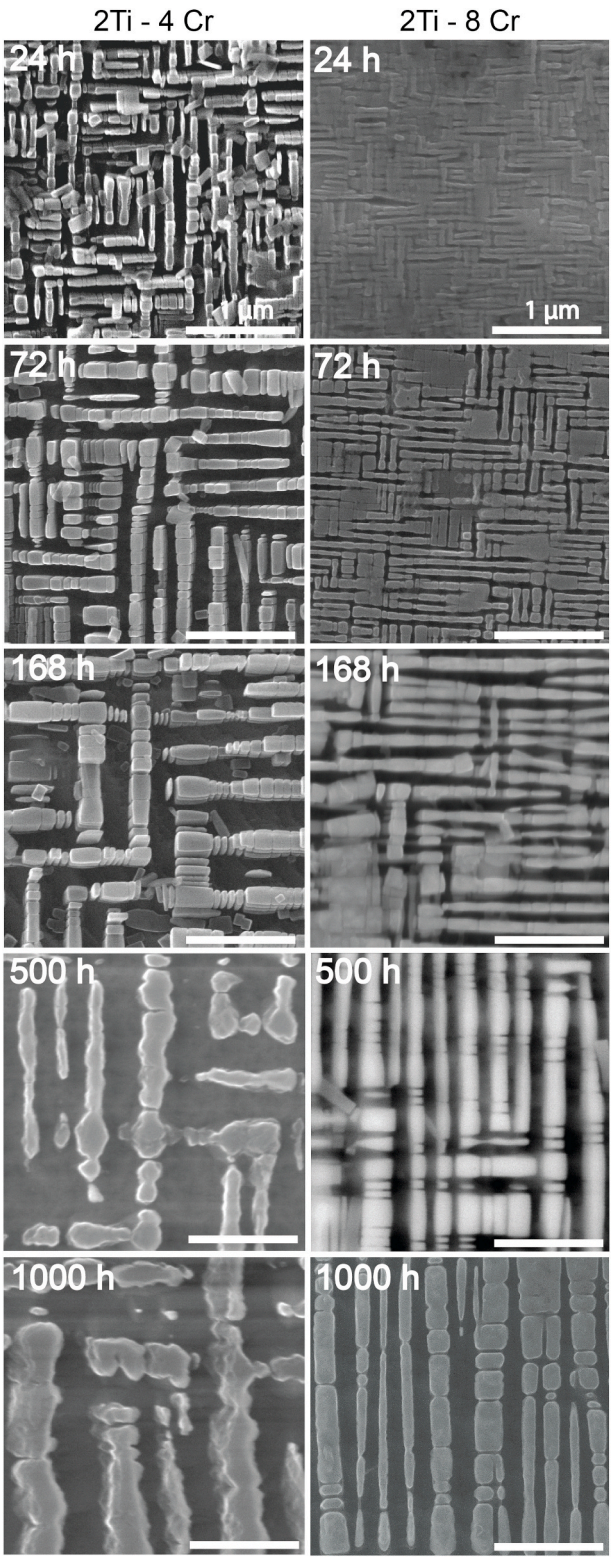

Fig. 3. SEM micrographs of Co–10Ni–5Al-xCr-3Nb–3V–2Ti-0.04B (x = 4 and 8, labeled 2Ti–4Cr and 2Ti–8Cr, respectively) aged at 850 °C between 24 and 1000 h, showing γ/γ′ microstructure.

Directional coarsening and coalescence has also previously been seen in Ni-based γ/γ′ alloys like Ni-Al [57], Ni-Ga and Ni–Ge [58]. As discussed by Ardell [58] and Cottura et al. [59], for Ni-based superalloys, the shape of precipitates can be determined by examining the effect of elastic interactions on microstructural evolution. Such elastic effects can originate from a difference in phase lattice constants, a differences in phase elastic constants, and/or from externally imposed stresses [60]. One of the key points of the study by Cottura et al. is that there is a relationship between the elastic energy within the γ channels and the elastic constant coefficient $C'=(C_{11}-C_{12})/2$, such that a lower inhomogeneity ($\Delta C'\approx 0$ between the two phases) leads to weaker elastic repulsions along the cubic directions and a stronger alignment of precipitates along soft elastic directions [59]. The resulting microstructure is analogous to that observed in our alloys, represented by sheets or plates composed of elongated γ′-precipitates separated by thin γ-channels with a large spacing between each sheet.

3.2. Atom probe tomography (APT) study

Atom Probe Tomography (APT) reconstructions for the 6Ti–0Cr, 6Ti–4Cr and 2Ti–8Cr alloys aged for 24 h at 850 °C are shown in Fig. 4a, b and c, respectively. Proximity histograms for each alloy, taking into consideration the average of all phases and precipitates, are also shown in Fig. 4. The APT tips consist of ~97, ~70 and ~190 million atoms for the 6Ti–0Cr, 6Ti–4Cr and 2Ti–8Cr alloys, respectively. The APT reconstruction in Fig. 4a (for 6Ti–0Cr) contains 11 partial γ′ nanoprecipitates (30–100 nm in size), with some having cuboidal and others having plate-like (50–100 nm in thickness) morphologies, consistent with microstructure SEM micrographs shown in Fig. 2. Similarly, in Fig. 4b (for 6Ti–4Cr), the tip contains 6 partial γ′ precipitates with a plate-like morphology. That plate-like morphology is less evident in 2Ti–8Cr (Fig. 4c), were the APT tip reconstructions contains 15 partial and 2 full γ′-precipitates which exhibit a directional alignment with a cuboidal morphology and a smaller size as compared to the other two alloys.

A summary of the APT results - including elemental partitioning, phase concentration and tip composition - can be found in Table 2. In 6Ti–0Cr, all alloying elements, except for cobalt, partition to the γ′-phase, and the elements showing the strongest partitioning are niobium ($K_{Nb}^{\gamma'/\gamma}=5.13$), boron ($K_{B}^{\gamma'/\gamma}=3.95$), and titanium ($K_{Ti}^{\gamma'/\gamma}=3.51$). The other three alloying elements show relatively low partitioning to the γ′ phase: vanadium ($K_{V}^{\gamma'/\gamma}=1.86$), nickel ($K_{Ni}^{\gamma'/\gamma}=1.66$), and aluminum ($K_{Al}^{\gamma'/\gamma}=1.26$). In 6Ti–4Cr, cobalt and chromium ($K_{Cr}^{\gamma'/\gamma}=0.68$) partition to the γ-phase while all other elements partition to the γ′-phase; again, the elements showing the strongest partitioning are niobium ($K_{Nb}^{\gamma'/\gamma}=3.83$), titanium ($K_{Ti}^{\gamma'/\gamma}=3.13$) and boron ($K_{B}^{\gamma'/\gamma}=2.98$). The other three alloying elements show relatively low partitioning to the γ′ phase: vanadium ($K_{V}^{\gamma'/\gamma}=1.59$), nickel ($K_{Ni}^{\gamma'/\gamma}=1.53$), and aluminum ($K_{Al}^{\gamma'/\gamma}=1.23$). Comparing these two alloys, the addition of 4 at. % Cr decreases the partitioning of Nb, V and Ti slightly, as illustrated in Fig. 5. For the low-Ti, high-Cr alloy (2Ti–8Cr), cobalt and chromium ($K_{Cr}^{\gamma'/\gamma}=0.50$) partition to the γ-phase with Cr showing a stronger partition to the γ-phase ($K_{Cr}^{\gamma'}=0.68$). As seen for the other two alloys, the elements showing the strongest partitioning to the γ′-phase are boron ($K_{B}^{\gamma'/\gamma}=6.96$), niobium ($K_{Nb}^{\gamma'/\gamma}=3.81$), and titanium ($K_{Ti}^{\gamma'/\gamma}=3.70$) and the other three alloying elements show low partitioning to the γ′ phase: vanadium ($K_{V}^{\gamma'/\gamma}=1.52$), nickel ($K_{Ni}^{\gamma'/\gamma}=1.47$), and aluminum ($K_{Al}^{\gamma'/\gamma}=1.43$). The latter alloy shows slight increases in partitioning tendency to the γ′-phase for Al, Ti and B, as seen in Fig. 5.

These results are consistent with the partitioning behavior displayed by other Co–Ta–V-based superalloys [9,10] where elements such as Nb and Ti are considered γ′-formers given their strong partitioning to that phase, while elements such as Ni and Al show weak partitioning between the two phases [27,36,47,61] and Cr has a strong preferential partitioning to the γ – phase [36,47,62,63]. Assuming that Co and Ni occupy the A-sublattice of the A_3B structure in these alloys and that all other elements occupy the B-sublattice, the γ′-phase stoichiometry can be calculated as $(Co_{0.85}Ni_{0.15})_3(Ti_{0.46}Al_{0.24}Nb_{0.18}V_{0.12}B_{0.001})$ for 6Ti–0Cr, $(Co_{0.86}Ni_{0.14})_3(Ti_{0.37}Al_{0.24}Cr_{0.15}Nb_{0.14}V_{0.10}B_{0.002})$ for 6Ti–4Cr and $(Co_{0.85}Ni_{0.15})_3(Ti_{0.13}Al_{0.25}\ Nb_{0.24}Cr_{0.21}V_{0.16}B_{0.01})$ for 2Ti–8Cr. This assumption is consistent with the Co and Ni concentrations in the γ′-phase adding to 74–76 at.% for the three above alloys (6Ti–0Cr, 6Ti–4Cr, and 2Ti–8Cr), but more detailed studies of site occupancy are needed to fully validate this hypothesis. By comparison, for ternary Co–Nb–V, the γ′- phase composition is $Co_3(Nb_{0.65}V_{0.35})$ [9]. For the binary and for the three multinary Co–Nb–V-based alloys, a similar Nb/V ≈ 1.5–1.8 ratio is present in the γ′- phase, indicating that Al, Ti and Cr do

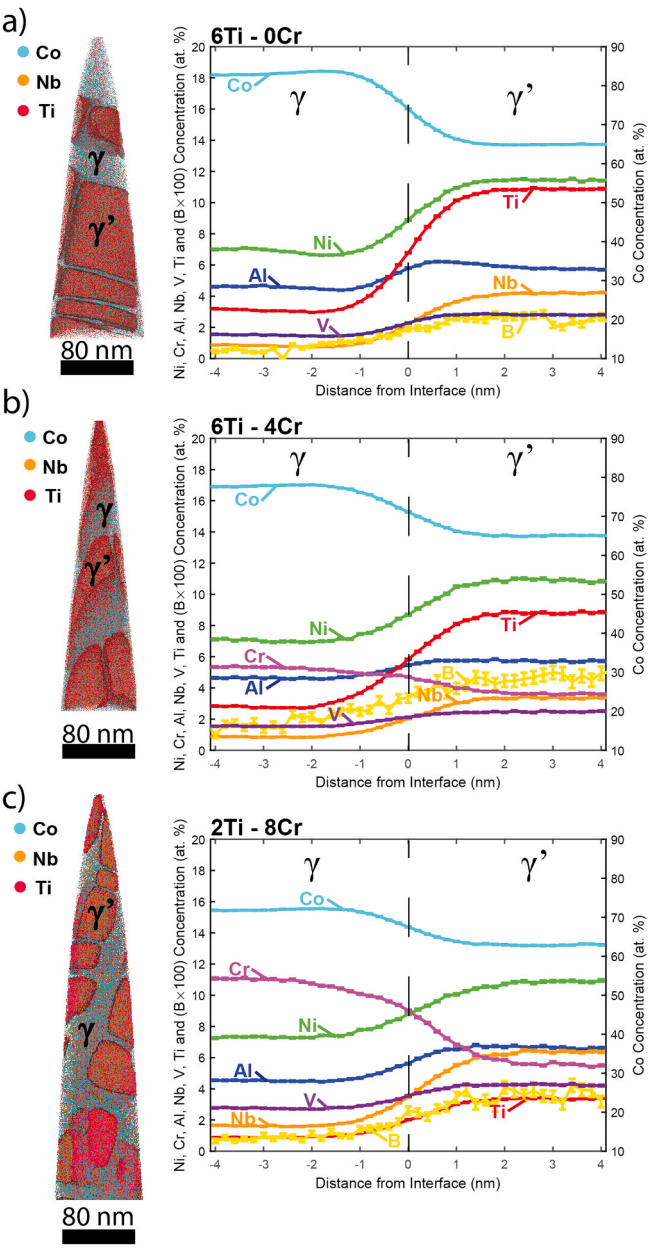

Fig. 4. APT tip reconstruction showing γ/γ′ microstructure in Co–10Ni–6Ti–5Al-xCr-3Nb–3V-0.04B (x = 0 and 4) and Co–10Ni–8Cr–5Al–3Nb–3V–2Ti-0.04B ((a) 6Ti–0Cr, (b) 6Ti–4Cr, and (c) 2Ti–8Cr) aged at 850 °C for 24 h, with their respective proxigrams showing elemental partitioning between γ and γ′ phases.

Table 2
APT concentration for tip (volume, γ- and γ′ phase, in at.%) and elemental partitioning coefficients ($K^{\gamma'/\gamma}$, dimensionless), as measured by APT for Co–10Ni–6Ti–5Al-xCr-3Nb–3V-0.04B (x = 0 and 4) and Co–10Ni–8Cr–5Al–3Nb–3V–2Ti-0.04B (6Ti–0Cr, 6Ti–4Cr and 2Ti–0Cr, respectively), after aging for 24 h at 850 °C.

Alloy		Elemental Composition(at %)							
		Co	Ni	Cr	Al	Nb	V	Ti	B
6Ti–0Cr	Bulk(Tip)	75.14	8.79	–	5.13	2.29	2.11	6.52	001
	γ	83.13	6.88	–	4.57	0.82	1.50	3.10	0.01
	γ′	64.93	11.45	–	5.73	4.20	2.79	10.87	0.03
	$k_i^{\gamma'/\gamma}$	0.78	1.66	–	1.26	5.13	1.86	3.51	3.95
6Ti–4Cr	Bulk (Tip)	72.48	8.59	4.67	5.14	1.91	1.97	5.21	0.03
	γ	77.71	7.07	5.32	4.64	0.87	1.56	2.81	0.02
	γ′	65.17	10.83	3.61	5.72	3.35	2.48	8.79	0.05
	$k_i^{\gamma'/\gamma}$	0.84	1.53	0.68	1.23	3.83	1.59	3.13	2.98
2Ti–8Cr	Bulk (Tip)	68.42	8.64	8.99	5.36	3.38	3.35	1.84	0.02
	γ	71.73	7.37	10.98	4.58	1.64	2.79	0.91	0.01
	γ′	63.19	10.83	5.54	6.55	6.25	4.23	3.37	0.04
	$k_i^{\gamma'/\gamma}$	0.88	1.47	0.50	1.43	3.81	1.52	3.70	6.96

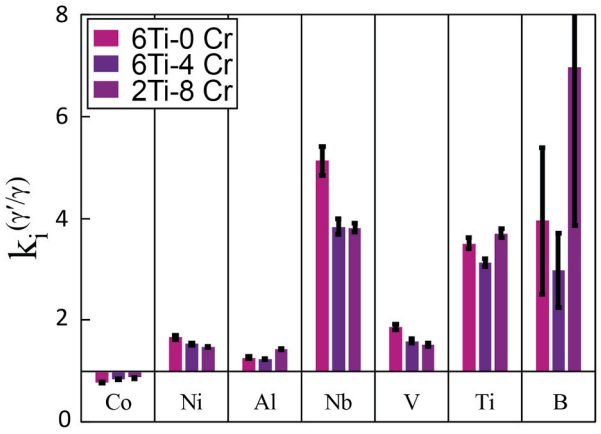

Fig. 5. Elemental partitioning between γ and γ′ phases for the three alloys shown in Fig. 4.

not preferentially replace either Nb or V in the B-sublattice of the $L1_2$ structure. The same behavior is seen in Co–Ta–V alloys modified with Al and Ti, where, in the ternary $Co_3(Ta_{0.76}V_{0.24})$, a ratio Ta/V ≈ 3 is found, and Al and Ti do not show a preference to replace either Ta or V in the B-sublattice of the $L1_2$ structure [9,10].

Using the lever rule, the γ' volume fraction for the different tips can be calculated based on the elemental concentrations and tip compositions as measured by APT (Table 2):

$$C_i^{\gamma'}\phi + C_i^{\gamma}(1-\phi) = C_i^{Bulk} \quad (2)$$

where ϕ is the γ′ volume fraction and C_i^{Bulk}, $C_i^{\gamma'}$ and C_i^{γ} are the concentrations of species i (i = Co, Ni, Al, Nb, V, Ti, B and Cr) in the bulk tip, γ′-phase and γ-phase, respectively. Rewriting Eq, (2), the γ′ volume fraction is:

$$\phi = \left(C_i^{Bulk} - C_i^{\gamma}\right)/\left(C_i^{\gamma'} - C_i^{\gamma}\right) \quad (3)$$

Thus, the γ′ volume fraction can be obtained by plotting $(C_i^{Bulk} - C_i^{\gamma})$ against $(C_i^{\gamma'} - C_i^{\gamma})$ for each element *i* and fitting a linear regression whose slope is equal to ϕ. The linear regressions are shown in Fig. S6 of supplemental information. The resulting tip γ′ volume fractions are 43.8 ± 1.6%, 41.4 ± 1.4%, and 38.0 ± 1.3% for 6Ti–0Cr, 6Ti–4Cr and 2Ti–8Cr, respectively. These measurement volumes are very small, ~5000 nm^3 (~7x7x100 nm). Metallographic measurements of γ' area fractions, made on SEM micrographs spanning tens of square micrometers, provide values of 53.3 ± 0.7%, 59 ± 0.5%, and 64 ± 3% for 6Ti–0Cr, 6Ti–4Cr and 2Ti–8Cr, respectively, and are more representative of the overall volume fraction.

3.3. Mechanical properties

3.3.1. Hardness at ambient temperature

Fig. 6 shows Vickers microhardness measurements of the 6Ti–0Cr, 6Ti–4Cr and 2Ti–8Cr alloys measured at room temperature for specimens aged at 850 °C for 0, 24, 72, 168, 500 and 1000 h. For all three alloys, the hardness is the same (2.6–2.9 GPa, within error) in the solution heat-treated condition (0 h). Hardness increases with the addition of Cr for all aging times, except for 6Ti–4Cr at 1000 h. At 1000 h, the microstructure in 6Ti–0Cr and 6Ti–4Cr is very similar (Fig. 2), which explains the similar hardness measurement. The 2Ti–8Cr alloy (Fig. 3) shows the highest hardness compared with 6Ti–0Cr and 6Ti–4Cr, consistent with its γ' precipitates being significantly less coarsened beyond 168 h of aging (Figs. 2–3).

All alloys show peak hardness at 72 h of aging. A similar behavior of increasing peak hardness with increasing Cr content was reported by Pandey et al. [30] in Co–30Ni–10Al–5Mo–2Ta–2Ti-xCr alloys (x = 0, 2, 5, and 8 at.% Cr) alloys aged at 900 °C. In these alloys, the hardness increases from ~3.1 GPa (for 2Cr) to ~3.3 GPa (for 8Cr) after 50 h of aging, and remains the same up to 1000 h. Replacing 4Ti for 4Cr (from

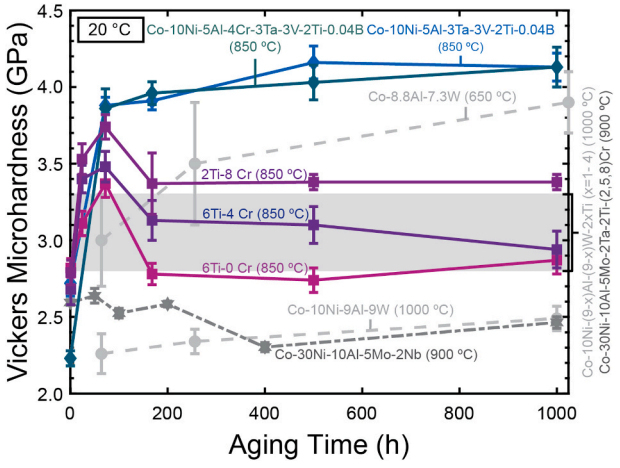

Fig. 6. Plot of Vickers microhardness (measured at 20 °C) as a function of aging time at 850 for Co–10Ni–6Ti–5Al-xCr-3Nb–3V-0.04B (x = 0 and 4, 6Ti–0Cr and 6Ti–4Cr) and Co–10Ni–8Cr–5Al–3Nb–3V–2Ti-0.04B (2Ti–8Cr), compared with various Co-based alloys from literature (corresponding aging temperatures are shown on plot).

6Ti–4Cr to 2Ti–8Cr) produces higher hardness. This may be due to Cr acting as a solid-solution strengthener in the γ-phase (based on APT partitioning coefficients), the increase amount of B in the γ′-phase making shearing more difficult, and/or slight changes in γ′-phase microstructure, affecting the motion of dislocations via precipitation strengthening.

For further comparison, microhardness measurements and measurement ranges for Co–10Ni–5Al–3Ta–3V–2Ti-0.04B-(0 and 4)Cr [10], Co–Al–W-based superalloys (Co-8.8Al.7.3W [64], Co–10Ni-(9-x) Al-(9-x)W-(2x)Ti (x = 0–4) [8]) and W-free Co-superalloys (Co–30Ni–10Al–5Mo–2Ta–2Ti-xCr (x = 2,5 and 8) [30], and Co–30 Ni–10Al–5Mo–2Nb [32]) are shown in Fig. 6. The highest hardness is seen in Co–Ta–V-based alloys [10], followed by Co-8.8Al.7.3W [64] which show similar hardness at short aging times (50 and 256 h of aging at 650 °C) and higher hardness at 1056 h of aging, close to peak-hardness; this peak aging is reached at much longer time than the present Co–V–Nb based alloys, consistent with the very slow diffusivity of W and Ta. For Co–Ta–V-based alloys, adding Cr to Co–10Ni–5Al–3Ta–3V–2Ti-0.04B does not affect hardness. Our 6Ti–0Cr, 6Ti–4Cr and 2Ti–8Cr alloys are in the same range of hardness as W-containing Co–10Ni-(9-x)Al-(9-x)W-(2x)Ti (x = 0–4) [8] and W-free Co–30Ni–10Al–5Mo–2Ta–2Ti-xCr (x = 2,5 and 8) [30] alloys where similar Ti and Cr amount are used. The lowest hardness is seen in Co–10Ni–9Al–9W [8] and Co–30Ni–10Al–5Mo–2Nb [8] which do not contain Cr or Ti acting as solid-solution strengtheners.

3.3.2. Creep properties at 850 °C

Fig. 7 shows the minimum creep strain rate $\dot{\varepsilon}$ as a function of compressive stress σ for the 6Ti–0Cr, 2Ti–4Cr and 2Ti–8Cr alloys tested at 850 °C. At high temperature (T > 0.5 T_M) and high stresses, the creep behavior of coarse-grained alloys is controlled by dislocation glide and climb and can be described by the Mukherjee-Bird-Dorn power-law equation [65,66]:

$$\dot{\varepsilon} = A\sigma^n \exp\left(\frac{-Q}{R_g T}\right) \quad (4)$$

where A is a constant, *n* is the stress exponent, Q is the activation energy (related to the activation energy for self-diffusion), R_g is the ideal gas constant, and T is the absolute temperature. For precipitation-strengthened alloys such as Ni- or Co-based superalloys, the stress exponent is usually well above the Ni- or Co-matrix solid-solution value (n_{ss} = 3–5), reflecting the presence of shearable, coherent γ′-precipitates which inhibit dislocation glide and climb [65,66]. Using a power-law fit in Fig. 7, the stress exponent *n* is found as n = 8.8 for 6Ti–0Cr, n = 8.4 for 2Ti–4Cr and n = 8.1 for 2Ti–8Cr. At 850 °C, the 6Ti–0Cr alloy shows the lowest creep resistance. The 2Ti–4Cr alloy shows an increase in creep resistance by about half an order of magnitude (as measured for strain rate at a given stress). Further additions of 4 at. % (from 2Ti–4Cr to 2Ti–8Cr) provides a slight increase in creep resistance, by a factor ~1.2.

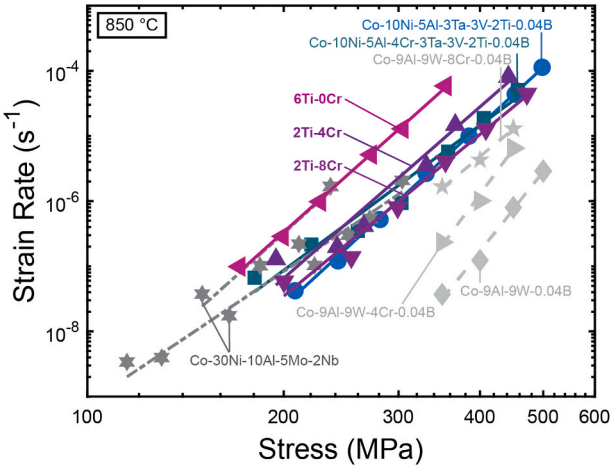

Fig. 7. Double logarithmic plot of minimum creep strain rate vs. compressive stress for Co–10Ni–6Ti–5Al–3Nb–3V-0.04B (6Ti–0Cr) and Co–10Ni-xCr-5Al–3Nb–3V–2Ti-0.04B (x = 4 and 8, 2Ti–4Cr and 2Ti–8Cr, respectively) alloys crept at 850 °C (after aging at 850 °C for 168 h), compared with various Co-based alloys crept at the same temperature, from literature [10,32,62].

The creep resistance of these Co–Nb–V-based superalloys is first compared to the previously studied W-free Co–10Ni–5Al–3Ta–3V–2Ti-0.04B-(0 and 4)Cr [10] alloys which contain the same amount of refractory elements (6 at.% Ta + V vs. 6 at.% Nb + V). When no Cr is present, the creep resistance of the 6Ti–0Cr alloy is about a factor ~1.75 lower than Co–10Ni–5Al–3Ta–3V–2Ti-0.04B; given that both superalloys contain a similar microstructure (coarsened and coalesced elongated γ′ precipitates with a volume fraction of 35–40%), the lower creep resistance of the 6Ti–0Cr alloy can be attributed to a lack of slow-diffusing Ta. When Cr is added to the alloys at the expense of 4 at.% Ti (from 6Ti–0Cr to 2Ti–4Cr and 2Ti–8Cr), the creep resistance is the same as for Co–10Ni–5Al–4Cr–3Ta–3V–2Ti-0.04B [10]. The creep resistance is also similar to that of W-free Co–30Ni–10Al–5Mo–2Nb (data are shown for two separate samples crept for different durations [32]) with slightly higher content of refractory elements (7 at.% Mo + Nb). Our Co–Nb–V-based alloys are in a similar range as the two tested samples. This is expected as the Co–30Ni–10Al–5Mo–2Nb alloys have a similar volume fraction (~35% vs. ~40% in Co–Nb–V alloys) and mass density (~8.12 vs. ~7.97–8.12 in Co–Nb–V alloys) [32]. Data are also shown in Fig. 7 for three W-bearing alloys: Co–9Al–9W-0.04B (58% γ′) [67], Co–9Al–9W–4Cr-0.04B (58% γ′) [62], Co–9Al–9W–8Cr-0.04B (64% γ′) [62]. In these W-bearing alloys, it is apparent that increasing Cr content (from 0 to 4 and 8 at. % Cr) decreases the creep resistance of the alloys, by ~2 orders of magnitude in the case of Co–9Al–9W–8Cr-0.04B [10,62]. This can be explained by a reduction in the lattice misfit as reported by Povstugar et al. [62] and possibly by the presence of other deleterious phases, such as the μ-phase, as reported by Bauer et al. in Cr-containing alloys [68]. As in Co–Ta–V alloys [10], Cr-containing Co–Nb–V-based alloys show a similar creep resistance to Co–9Al–9W–8Cr-0.04B, despite having a much lower density (~8.1 vs. 9.2 g/cm^3) and lower γ′ volume fraction (~40 vs. ~64%) than the W-bearing alloy. In contrast to the above W-bearing alloys, Cr in our Co–Nb–V-based alloys (2Ti–4Cr and 2Ti–8Cr) has a minimal effect on the creep resistance of the alloy. A similar behavior was seen in more complex Co–Al–W based alloys [69,70] when adding 4 and 8 at.% Cr to Co–30Ni–11Al–2Ti-5.5W-2.5Ta-0.1B [69] and Co–30Ni–7Al–4Ti–3 Mo–2W–1Nb–1Ta-0.1B-xCr [70] alloys [10,69,70].

The post-creep microstructures of the 6Ti–0Cr, 2Ti–4Cr and 2Ti–8Cr alloys, subjected to 43, 24 and 30 h of creep, respectively, are shown in Fig. 8 in cross-sections perpendicular and parallel to the compressive load. Rafting, characterized by horizontal rows of coalesced and irregular γ' precipitates in the direction perpendicular to the applied load, is seen in the 6Ti–0Cr and 2Ti–4Cr alloys, while rafting in both directions (perpendicular and parallel to the applied load) is observed in the 2Ti–8Cr alloys. A similar effect was reported in Co–Ta–V-based alloys where Co–10Ni–5Al–3Ta–3V–2Ti-0.04B shows rafts in directions perpendicular to the applied stress while Co–10Ni–5Al–4Cr–3Ta –3V–2Ti-0.04B shows rafts in both directions [10]. Rafting in the perpendicular direction to the applied load is indicative of a positive lattice mismatch, consistent with other Co-based superalloys [10,32,61, 69–73].

3.4. Oxidation resistance

Isothermal oxidation tests were performed at 850 °C for 20 h to study the oxidation resistance of the alloys, focusing on the effect of Cr by comparing the 6Ti–0Cr and 6Ti–4Cr alloys; tests on 2Ti–8Cr provide information on the alloy with the highest Cr content and the best creep resistance and hardness. Fig. 9 shows backscatter electron micrographs

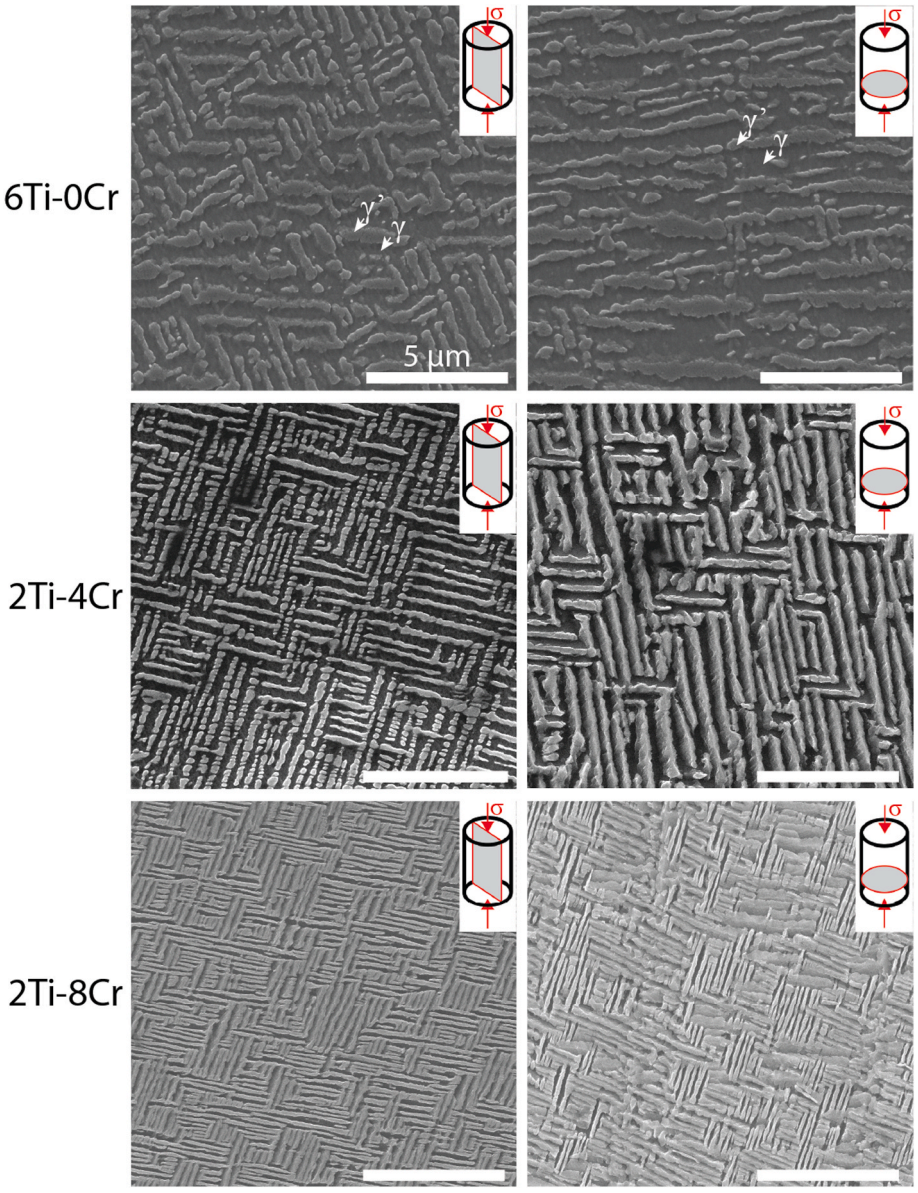

Fig. 8. SEM micrographs showing partial γ′-rafting in cross-sections parallel (first column) and perpendicular (second column) to the applied load for the three alloys shown in Fig. 7, after creep at 850 °C for 19 h up to 354 MPa (6Ti–0Cr), for 24 h up to 442 MPa (2Ti–4Cr) and for 30 h up to 472 MPa (2Ti–8Cr).

of cross-sections, showing the surface oxide structure in 6Ti–0Cr, 6Ti–4Cr and 2Ti–8Cr alloys after oxidation. Fig. S7 shows the elemental distribution of all elements across the different oxide scales. Multiple distinct oxide layers are present, which are representative of typical oxidations surfaces composed of (i) an outermost oxide scale followed by (ii) a layer of mixed oxides (dependent on alloying additions), (iii) an oxide intrusion zone, (iv) a precipitate-depletion zone, before reaching (v) the substrate [43,74]. The oxide scale is deepest in the low Cr (6Ti-0/4Cr) alloys, and significantly shallower for the high Cr (2Ti–8Cr) alloy. Based on EDS maps (Fig. S7), for all alloys, the outermost scale is composed mainly of Co and O atoms, indicating of cobalt oxide. The second layer contains a mix of different oxides as it contains Co, Al, Ti, Nb, V (and Cr for the Cr containing alloys) as well as O atoms. The third layer shows intrusion of the different oxides seen in the second layer followed by a thin Ni-rich γ′-depletion zone before reaching the bulk which is composed of a γ-γ′ microstructure. The composition of the different oxide scales was determined based on the qualitative elemental maps obtained by EDS and reported oxide layers in literature related to Co-based superalloys. The first layer is porous in nature and is representative of CoO or Co_3O_4 which are the two stable oxides at temperatures near 800 °C [41–43,75–81]; Co_3O_4 is known to decompose into CoO at temperatures higher than 900 °C [43,75–78,80,82]. These oxides have high oxygen diffusivities, therefore, they are not effective at preventing further oxidation [83]. The second layer contains multiple oxides, as all alloying elements (CO, Al, Ti, Nb, Cr and V) except for Ni are present. This behavior is similar to that seen in other Co-based superalloys where the top layer is composed by CoO/Co_3O_4 and the following layer is composed of fine grains of mixed oxides including: Al- and W-rich oxides for Co–Al–W-based alloys [43,76,78,80,82] and Ta-, Al- and Mo-rich oxides for W-free Co–Al–Mo–Ta alloys [77]. The third layer shows intrusion of the mixed oxides into the Ni-rich depletion zone as seen by Klein et al. [81] and Weiser et al. [42] in Co–9Ni–9Al–9W-0.12B and Co-37.5Ni–9Al–8W (at. %) superalloys, respectively. None of our alloys formed a continues protective Al_2O_3 or Cr_2O_3 layer, suggesting that higher content of Al and Cr are needed for better oxidation resistance. Nevertheless, the much smaller oxidation depth visible in 2Ti–8Cr can be attributed to both the higher Cr content and the lower amount of Ti, which is known to diminish the oxidation

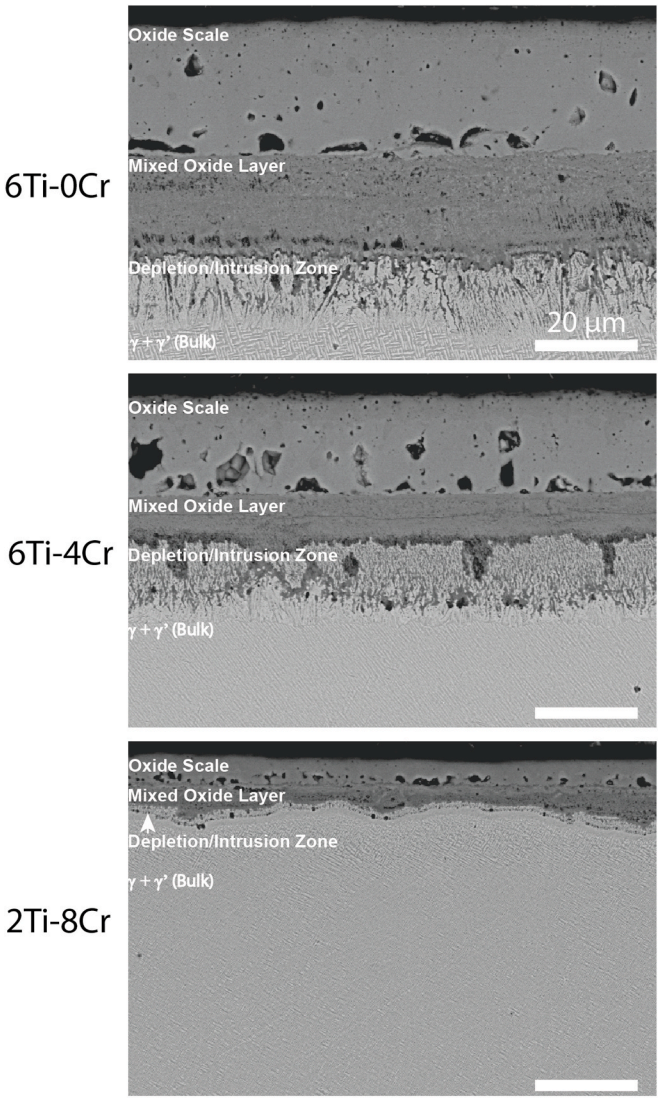

Fig. 9. SEM micrographs of cross-sections, showing surface oxide layers (with elemental maps obtained by EDS given in supplemental information), after 20 h of isothermal oxidation at 850 °C for three alloys previously aged at 850 °C for 24 h: (a) 6Ti–0Cr (Co–10Ni–6Ti–5Al–3Nb–3V-0.04B); (b) 6Ti–4Cr, (Co–10Ni–6Ti–5Al–4Cr–3Nb–3V-0.04B) and (c) 2Ti–8Cr (Co–10Ni–8Cr–5Al–3Nb–3V–2Ti-0.04B).

resistance as vacancies are introduced by Ti ions when doping Al_2O_3 [84] and Cr_2O_3 [85].

To compare the oxidation resistance of the different alloy, the mass gain per unit area Δm was plotted against time (Fig. 10a). The highest mass gain is seen in the Cr-free 6Ti–0Cr alloy (~5.5 mg/cm^2 after 20 h), decreasing moderately by the addition of 4%Cr in the 6Ti–4Cr alloy (3.9 mg/cm^2), and strongly decreasing (to ~1.5 mg/cm^2) for 2Ti–8Cr, due to a simultaneous decrease of Ti and increase of Cr. The oxidation of most alloys follows a parabolic growth behavior [86] according to:

$$(\Delta m)^2 = kt \quad (5)$$

where Δm represents mass gain due to oxide content, k is the parabolic rate constant and t is time. Transient oxidation (non-linear regions) takes place at early oxidation times. For consistency in extracting the oxidation rate constants, transient oxidation is assumed to be taking place in the first 10 h, with the next 10 h following a steady-state parabolic growth. The extracted parabolic rates constants k are shown as a function of Cr content in Fig. 10b, also showing the measured oxide

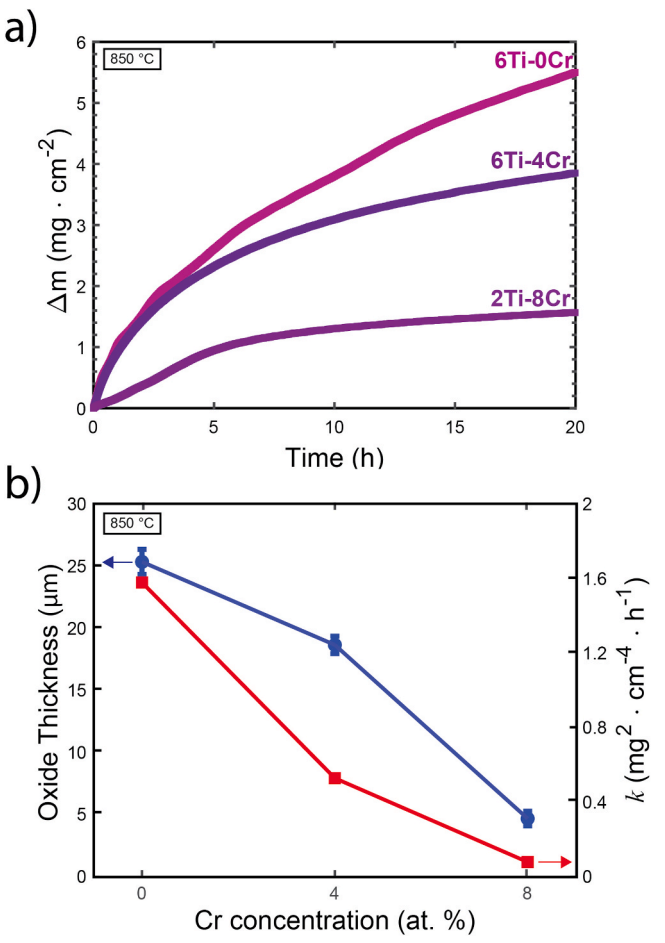

Fig. 10. (a) Plot of mass gain as a function of time during isothermal oxidation at 850 °C for three alloys shown in Fig. 9, previously aged at 850 °C for 24 h. (b) Plot of oxide scale thickness and parabolic rate constant, k, as a function of Cr concentration, for the three alloys shown in (a).

scale thicknesses after 20h. The parabolic rate constants of each alloy are $k_{6Ti-0Cr} = 1.58$, $k_{6Ti-4Cr} = 0.53$ and $k_{2Ti-8Cr} = 0.08$ mg^2/cm^4 h (Fig. S8). The ranking of these k values is consistent with the oxide scale micrographs (Fig. 9), from which the oxide scale thickness d was measured for each alloy as: $d_{6Ti-0Cr} = 25.3 \pm 1.0$, $d_{6Ti-4Cr} = 18.6 \pm 0.7$ and $d_{2Ti-8Cr} = 4.6 \pm 0.6$ μm. However, none of these alloys showed the formation of Al_2O_3 or Cr_2O_3 which are known to exhibit a low oxygen ion diffusivity that very effectively protects the alloy surface from further oxidation [41,43,69,87]. Increasing the Al and Cr amount might lead to the formation of Al_2O_3 and Cr_2O_3, but possibly at the cost of forming additional deleterious phases, beside the γ′ phase, within the grains or at grain boundaries.

3.5. γ′ solvus temperature and mass density

The solvus temperature of the 6Ti–0Cr, 6Ti–4Cr and 2Ti–8Cr alloys was measured as 977 ± 5, 1008 ± 1 and 953 ± 1 °C, via differential scanning calorimetry (DSC). Solvus temperatures are visible as a sharp exothermic peak in the DSC cooling curves which are shown in Fig. S9 of Supplementary Information. In Fig. 11a, the solvus temperature of 6Ti–0Cr, 6Ti–4Cr and 2Ti–8Cr alloys are compared to published alloys: the two Co–Ta–V-based alloys from our previous study (Co–10Ni–5Al-(0 and 4)Cr–3Ta–3V–2Ti-0.04B) [10], the W-bearing Co–9Al-9.8W [16] and two W-free alloys (Co–30Ni–10Al–5Mo–2Nb–2Ti [17] and Co–30Ni–10Al–5Mo–2Ta–2Ti [16]). Comparing the 6Ti–0Cr and the 6Ti–4Cr alloys with each other, it is apparent that the addition of Cr raised the solvus by ~30 °C, from 977 °C to 1008 °C. The latter

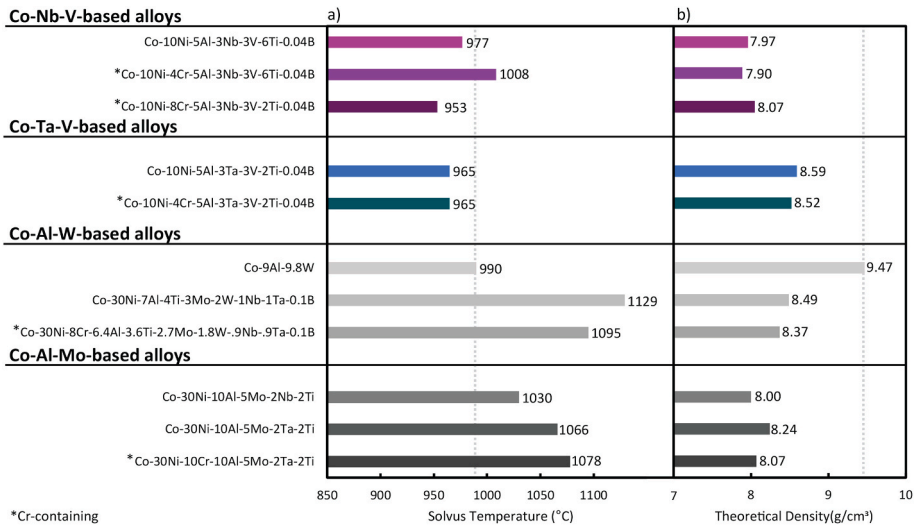

Fig. 11. (a) Solvus temperatures for Co–10Ni–6Ti–5Al-xCr-3Nb–3V-0.04B (x = 0 and 4) and Co–10Ni–8Cr–5Al–3Nb–3V–2Ti-0.04B alloys and (b) theoretical density for above alloys. Also shown are values for three W-bearing Co-based superalloys and five W-free Co-based superalloys from literature (Co–Ta–V-based and Co–Mo–Nb/Ta-based) [10,16,28,69].

temperature is similar to the solvus temperature of 1005 °C displayed by binary Co–12Ti [19]. Our solvus temperatures are lower than other W-free ternary alloys with high amounts of Ti or V: Co–5Ti–15V (1091 °C) [21] and Co–11Ti–15Cr (1100 °C) [18]. Both of these ternary alloys have some of the highest solvus temperatures seen in W-free Co-based alloys (apart from the 1242 °C solvus reported by Chen et al. in a Co–30Ni–10Al–5V–4Ta–2Ti alloy [22]) and are derivative of the Co–12Ti binary system, but (i) do not contain Al, which is a necessary element for oxidation resistance [1,10] and (ii) contain very high amounts of high-melting V, which is known to reduce oxidation and corrosion resistance at high temperatures [88]. In Co–5Ti–15V (1091 °C) [21] and Co–11Ti–15Cr (1100 °C) [18], improvement in solvus temperatures of ~90 °C are seen for both V and Cr additions, which suggest that increasing the amount of Cr or V in our alloys might lead to further improvement in solvus temperatures. In our 2Ti–8Cr alloy, the Cr amount is increased by 4 at. % directly replacing 4 at. % Ti, and the decrease in Ti is leads to a decrease in solvus temperature of ~50 °C, consistent with the premise that Ti improves strongly solvus temperatures [10]. Comparing with Al-containing Co-based superalloys (Fig. 11a), our 6Ti–0Cr and 6Ti–4Cr alloys have higher solvus temperatures than our previous Co–Ta–V based alloys [10], most probably due to the high Ti amounts. Furthermore, our alloys show similar solvus temperatures to Co–9Al-9.8W (990 °C) [16] but lower solvus temperatures than W-free Co–30Ni–10Al–5Mo–2Ti-2x (x = Ta or Nb) alloys, each with 30 at. % Ni, which have significantly higher solvus temperatures (1030 and 1066 °C) [16,17]. Our 2Ti–4Cr alloy has the lowest solvus temperature of all alloys compared Fig. 11a. As mentioned before, based on our result and the solvus temperatures seen in Co-Ti-Cr [18] and Co–Ti–V [21] ternary systems, increases in Cr and V content might lead to the higher solvus temperatures. Furthermore, based on studies on Co–Al–Mo-based alloys [16,17] increases in Ni content might also lead to higher solvus temperatures [10].

In Fig. 11b the calculated theoretical mass density (based on composition, density and atomic weight) of our 6Ti–0Cr, 6Ti–4Cr and 2Ti–8Cr alloys is compared with the five alloys used for comparison in Fig. 11a. For consistency and accurate comparison, the densities for the five alloys were also calculated and are expected to be somewhat different from those reported experimentally. Our alloys show significantly lower theoretical densities than W-containing Co–9Al-9.8W and Ta-containing Co–Ta–V-based alloys, and similar densities to the other multinary W-free alloys, due to the high content of the relatively lightweight elements Ti, V, Cr, and Nb (4.5, 6.1, 7.1 and 8.6 g/cm^3, respectively) as compared to Ta and W (16.6 and 19.2 g/cm^3, respectively). Although the alloys containing a high amount of low-density Ti (6Ti–0Cr and 6Ti–4Cr) showed the lowest density, these also exhibit significant coalescence of precipitates during aging and lower hardness and creep resistance (6Ti–0Cr), which makes the 2Ti–4Cr and 2Ti–8Cr more attractive for further development. Furthermore, increasing Cr content in 2Ti-xCr alloys will help decrease the density of the alloy (as seen in Co–Ta–V-based alloys [10]), while improving stability, oxidation resistance and creep resistance.

4. Summary

We report here that the metastable γ′- $Co_3(Nb_{0.65}V_{0.35})$ phase recently discovered in the Co–6Nb–6V (at. %) ternary alloy [9] can be stabilized with the same elemental alloying additions (Al, Ti and Ni) as in Co–Ta–V-based ternary alloys [10]. We develop six multinary Co–Nb–V-based alloys with increasing alloying additions, and create Co–Nb–V-based alloys modified with elements (Cr, Ti, Al) which are lighter than Co, achieving for the first time Co-based γ/γ′ superalloys that are completely free of the high-density refractory elements Mo, Ta and W. Our final alloys show good creep- and oxidation resistance while maintaining a low mass density (~8.0 g/cm^3). Our conclusions are summarized in order of compositional complexity.

- For the first quaternary alloy, the ternary Co–6Nb–6V alloy was modified to include Al so as to stabilize the γ′-phase (and provide oxidation resistance), by replacing half the Nb and V with Al. The resulting Co–6Al–3Nb–3V composition shows no improvements as compared to Co–6Nb–6V and the microstructure is composed of $D0_{19}$-needle precipitates embedded in a γ-matrix.
- For the second quinary alloy, the first Co–6Al–3Nb–3V alloy was modified to replace 1 at. % Al for 1 at.% Ti. The resulting Co–5Al–3Nb–3V–1Ti alloy exhibits both γ′- and $D0_{19}$-phases embedded in a γ-matrix, showing that Ti is effective at stabilizing the γ′-phase. The microstructure is like that seen in Co–6Nb–6V after homogenization at 1300 °C followed by furnace cooling subsequently aged at 900 °C for 2 h and water quenched.
- Based on the previous two alloys and prior results from Co–Ta–V-based alloys [10], the third alloy was made by increasing the Ti concentration to 6 at. % while adding 10 at. % Ni and 0.04% B as compared to the above second alloy. This Co–10Ni–6Ti–5Al–3Nb–3V-0.04B alloy shows a stable γ+γ′

microstructure up to 1000 h at 850 °C. No other phases are seen in grains or at grain boundaries, where occasional coarsened grain boundary γ′-precipitates are present. This represents a dramatic improvement over the prior Co–6Nb–6V where metastable γ′-precipitates are only seen in the homogenized, furnace-cooled state before and after aging at 900 °C for 2 h, coexisting with needle-like $D0_{19}$ precipitates. This is also the first report of a low-density Co–Nb–V–Al-based γ+γ′ superalloy, which is free of high-density W and Ta, as well as medium-density Mo.

- For the fourth alloy, Cr is added at 4 at. % to form a Co–10Ni–6Ti–5Al–4Cr–3Nb–3V-0.04B alloy. This γ+γ′ alloy does not show any significance microstructure changes in comparison with the third Cr-free alloy when aged up to 1000 h at 850 °C. There is a slight increase in hardness, solvus and oxidation resistance as 4 at. % Cr is added.
- The fifth alloy was created by reducing the amount of Ti to form a Co–10Ni–5Al–4Cr–3Nb–3V–2Ti-0.04B alloy and a sixth alloy was created by adding an additional 4 at.% Cr to form Co–10Ni–8Cr–5Al–3Nb–3V–2Ti-0.04B. Both these alloys (with 2 at. % Ti) show better microstructural stability, producing γ′-precipitates with regular cuboidal morphologies arranged into sheets, as compared the third and fourth alloys (with 6 at. % Ti), and they exhibit a slight increase in γ′ volume fraction and a slight decrease in γ′ size in the early aging stages (168 h at 850 °C).
- The sixth alloy, with the highest Cr content, displays the highest hardness, creep resistance and oxidation resistance in this study. The creep resistance of this alloy at 850 °C, is similar to those of the following literature Co-based superalloys: (i) Ta- and V-bearing Co–10Ni–5Al–3Ta–3V–2Ti-0.04B-(0 and 4)Cr, (ii) Mo- and Nb-bearing Co–30Ni–10Al–5Mo–2Nb, and (iii) W-bearing Co–9Al–9 W–8Cr alloys.
- For Co–10Ni–6Ti–5Al–3Nb–3V-0.04B, Co–10Ni–6Ti–5Al–4Cr–3 Nb–3V-0.04B and Co–10Ni–8Cr–5Al–3Nb–3V–2Ti-0.04B aged for 24 h at 850 °C, the composition of the cuboidal γ′-precipitates is measured by atom probe tomography as $(Co_{0.85}Ni_{0.15})_3(Ti_{0.46}Al_{0.24}Nb_{0.18}V_{0.12}B_{0.001})$, $(Co_{0.86}Ni_{0.14})_3(Ti_{0.37}Al_{0.24}Cr_{0.15}Nb_{0.14}V_{0.10}B_{0.002})$ and $(Co_{0.85}Ni_{0.15})_3(Ti_{0.13}Al_{0.25}Nb_{0.24}Cr_{0.21}V_{0.16}B_{0.01})$, respectively, assuming full partioning to the A and B sublattices. Al and Ti thus replace at a similar rate both Nb and V in the ternary metastable $Co_3(Nb_{0.65}V_{0.35})$ present in the original Co–6Nb–6V (at. %) alloy [9].

Data availability

The raw/processed data required to reproduce these findings cannot be shared at this time due to legal and technical/time limitations.

CRediT authorship contribution statement

Fernando L. Reyes Tirado: Conceptualization, Investigation, Formal analysis, Writing - original draft, Visualization. **Spencer V. Taylor:** Investigation. **David C. Dunand:** Conceptualization, Project administration, Writing - review & editing, Supervision.

Declaration of competing interest

The authors declare that they have no known competing financial interests or personal relationships that could have appeared to influence the work reported in this paper.

Acknowledgements

This study was supported by the U.S. Department of Commerce, National Institute of Standards and Technology, as part of the Center for Hierarchical Materials Design (CHiMaD) at Northwestern University (NU) via award 70NANB14H012. F.L.R.T acknowledges the support of a NSF Graduate Research Fellowship. S.T. acknowledges the support of the NU-MRSEC Research Experience for Undergraduates (NSF DMR-1720139) and the 3M Corporation. Atom-probe tomography was performed at the Northwestern University Center for Atom-Probe Tomography (NUCAPT). The LEAP tomograph at NUCAPT was purchased and upgraded with grants from the NSF-MRI (DMR-0420532) and ONR-DURIP (N00014-0400798, N00014-0610539, N00014-0910781, N00014-1712870) programs. NUCAPT received support from the MRSEC program (NSF DMR-1720139) at the Materials Research Center, the SHyNE Resource (NSF ECCS-1542205), and the Initiative for Sustainability and Energy (ISEN) at Northwestern University. This work made use of the MatCI Facility which receives support from the MRSEC Program (NSF DMR- 1720139) of the Materials Research Center at Northwestern University; the EPIC facility of Northwestern University's NUANCE Center, which has received support from the Soft and Hybrid Nanotechnology Experimental (SHyNE) Resource (NSF ECCS-1542205); the MRSEC program (NSF DMR-1720139) at the Materials Research Center; the International Institute for Nanotechnology (IIN); the Keck Foundation; the State of Illinois, through the IIN. The authors gratefully acknowledge experimental assistance from Mr. Brandon Ohl, Dr. Ding-Wen Chung, Dr. Richard Michi, Dr. Fei Xue and Dr. Amir Farkoosh (NU) and useful discussions with Dr. Ding-Wen Chung and Prof. D.N. Seidman (NU). S.T. thanks Prof. Marcus Young (University of North Texas) for use of DSC equipment.

Appendix A. Supplementary data

Supplementary data to this article can be found online at https://doi.org/10.1016/j.msea.2020.139977.

References

[1] R.C. Reed, The Superalloys: Fundamentals and Applications - Roger C. Reed - Google Books, Cambridge University Press, 2006, https://doi.org/10.1016/j.laa.2011.01.014.
[2] W. Huang, Y.A. Chang, A thermodynamic analysis of the Ni-Al system, Intermetallics 6 (1998) 487–498, https://doi.org/10.1016/S0966-9795(97)00099-X.
[3] M. Durand-Charre, J.H. Davidson, The Microstructure of Superalloys, Routledge, 1998, https://doi.org/10.1201/9780203736388.
[4] C.T. Sims, N.S. Stoloff, W.C. Hagel, Superalloys II, in: Superalloys II, 1987, p. 615, https://doi.org/10.1080/10426919208947432.
[5] J. Sato, T. Omori, K. Oikawa, I. Ohnuma, R. Kainuma, K. Ishida, Cobalt-base high-temperature alloys, Science 80 (312) (2006) 90–91, https://doi.org/10.1126/science.1121738.
[6] C.L. Lee, Precipitation-Hardening Characteristics of Ternary Cobalt-Aluminum-X Alloys, The University of Arizona, 1971.
[7] P.J. Bocchini, C.K. Sudbrack, D.J. Sauza, R.D. Noebe, D.N. Seidman, D.C. Dunand, Effect of tungsten concentration on microstructures of Co-10Ni-6Al-(0,2,4,6)W-6Ti (at%) cobalt-based superalloys, Mater. Sci. Eng. A 700 (2017) 481–486, https://doi.org/10.1016/j.msea.2017.06.018.
[8] P.J. Bocchini, C.K. Sudbrack, R.D. Noebe, D.C. Dunand, D.N. Seidman, Effects of titanium substitutions for aluminum and tungsten in Co-10Ni-9Al-9W (at%) superalloys, Mater. Sci. Eng. A 705 (2017) 122–132, https://doi.org/10.1016/j.msea.2017.08.034.
[9] F.L. Reyes Tirado, J. Perrin Toinin, D.C. Dunand, γ+γ′ microstructures in the Co-Ta-V and Co-Nb-V ternary systems, Acta Mater. 151 (2018) 137–148, https://doi.org/10.1016/j.actamat.2018.03.057.
[10] F.L. Reyes Tirado, S. Taylor, D.C. Dunand, Effect of Al, Ti and Cr additions on the γ-γ' microstructure of W-free Co-Ta-V-Based superalloys, Acta Mater. 172 (2019) 44–54, https://doi.org/10.1016/J.ACTAMAT.2019.04.031.
[11] M. Ooshima, K. Tanaka, N.L. Okamoto, K. Kishida, H. Inui, Effects of quaternary alloying elements on the γ′ solvus temperature of Co-Al-W based alloys with fcc/L12 two-phase microstructures, J. Alloys Compd. 508 (2010) 71–78, https://doi.org/10.1016/j.jallcom.2010.08.050.
[12] D.J. Sauza, D.C. Dunand, D.N. Seidman, Microstructural evolution and high-temperature strength of a γ(f.c.c.)/γ'(L12) Co–Al–W–Ti–B superalloy, Acta Mater. 174 (2019) 427–438, https://doi.org/10.1016/J.ACTAMAT.2019.05.058.
[13] D.J. Sauza, P.J. Bocchini, D.C. Dunand, D.N. Seidman, Influence of ruthenium on microstructural evolution in a model Co-Al-W superalloy, Acta Mater. 117 (2016) 135–145, https://doi.org/10.1016/j.actamat.2016.07.014.
[14] S.K. Makineni, B. Nithin, K. Chattopadhyay, A new tungsten-free γ-γ' Co-Al-Mo-Nb-based superalloy, Scripta Mater. 98 (2015) 36–39, https://doi.org/10.1016/j.scriptamat.2014.11.009.

[15] S.K. Makineni, B. Nithin, K. Chattopadhyay, Synthesis of a new tungsten-free γ-γ′ Cobalt-based superalloy by tuning alloying additions, Acta Mater. 85 (2015) 85–94, https://doi.org/10.1016/j.actamat.2014.11.016.

[16] S.K. Makineni, A. Samanta, T. Rojhirunsakool, T. Alam, B. Nithin, A.K. Singh, R. Banerjee, K. Chattopadhyay, A new class of high strength high temperature Cobalt based γ-γ′ Co-Mo-Al alloys stabilized with Ta addition, Acta Mater. 97 (2015) 29–40, https://doi.org/10.1016/j.actamat.2015.06.034.

[17] S.K. Makineni, B. Nithin, D. Palanisamy, K. Chattopadhyay, Phase evolution and crystallography of precipitates during decomposition of new "tungsten-free" Co (Ni)–Mo–Al–Nb γ–γ′ superalloys at elevated temperatures, J. Mater. Sci. 51 (2016) 7843–7860, https://doi.org/10.1007/s10853-016-0026-1.

[18] C.H. Zenk, I. Povstugar, R. Li, F. Rinaldi, S. Neumeier, D. Raabe, M. Göken, A novel type of Co–Ti–Cr-base γ/γ′ superalloys with low mass density, Acta Mater. 135 (2017) 244–251, https://doi.org/10.1016/j.actamat.2017.06.024.

[19] H.J. Im, S.K. Makineni, B. Gault, F. Stein, D. Raabe, P.P. Choi, Elemental partitioning and site-occupancy in γ/γ′ forming Co-Ti-Mo and Co-Ti-Cr alloys, Scripta Mater. 154 (2018) 159–162, https://doi.org/10.1016/j.scriptamat.2018.05.041.

[20] J.J. Ruan, C.P. Wang, C.C. Zhao, S.Y. Yang, T. Yang, X.J. Liu, Experimental investigation of phase equilibria and microstructure in the Co-Ti-V ternary system, Intermetallics 49 (2014) 121–131, https://doi.org/10.1016/j.intermet.2014.01.011.

[21] J.J. Ruan, X.J. Liu, S.Y. Yang, W.W. Xu, T. Omori, T. Yang, B. Deng, H.X. Jiang, C. P. Wang, R. Kainuma, K. Ishida, Novel Co-Ti-V-base superalloys reinforced by L12-ordered γ′ phase, Intermetallics 92 (2018) 126–132, https://doi.org/10.1016/j.intermet.2017.09.015.

[22] Y. Chen, C. Wang, J. Ruan, T. Omori, R. Kainuma, K. Ishida, X. Liu, High-strength Co–Al–V-base superalloys strengthened by γ′-Co3(Al,V) with high solvus temperature, Acta Mater. 170 (2019) 62–74, https://doi.org/10.1016/J.ACTAMAT.2019.03.013.

[23] G. Feng, H. Li, S.S. Li, J.B. Sha, Effect of Mo additions on microstructure and tensile behavior of a Co–Al–W–Ta–B alloy at room temperature, Scripta Mater. 67 (2012) 499–502, https://doi.org/10.1016/J.SCRIPTAMAT.2012.06.013.

[24] J. Koßmann, T. Hammerschmidt, S. Maisel, S. Müller, R. Drautz, Solubility and ordering of Ti, Ta, Mo and W on the Al sublattice in L12-Co3Al, Intermetallics 64 (2015) 44–50, https://doi.org/10.1016/J.INTERMET.2015.04.009.

[25] M. Jin, N. Miao, W. Zhao, J. Zhou, Q. Du, Z. Sun, Structural stability and mechanical properties of Co 3 (Al, M) (M = Ti, V, Cr, Zr, Nb, Mo, Hf, Ta, W) compounds, Comput. Mater. Sci. 148 (2018) 27–37, https://doi.org/10.1016/j.commatsci.2018.02.015.

[26] H.J. Zhou, F. Xue, H. Chang, Q. Feng, Effect of Mo on microstructural characteristics and coarsening kinetics of γ' precipitates in Co–Al–W–Ta–Ti alloys, J. Mater. Sci. Technol. 34 (2018) 799–805, https://doi.org/10.1016/J.JMST.2017.04.012.

[27] E.A. Lass, D.J. Sauza, D.C. Dunand, D.N. Seidman, Multicomponent γ'-strengthened Co-based superalloys with increased solvus temperatures and reduced mass densities, Acta Mater. 147 (2018) 284–295, https://doi.org/10.1016/j.actamat.2018.01.034.

[28] B. Nithin, A. Samanta, S.K. Makineni, T. Alam, P. Pandey, A.K. Singh, R. Banerjee, K. Chattopadhyay, Effect of Cr addition on γ–γ′ cobalt-based Co–Mo–Al–Ta class of superalloys: a combined experimental and computational study, J. Mater. Sci. 52 (2017) 11036–11047, https://doi.org/10.1007/s10853-017-1159-6.

[29] Q. Yao, S.-L. Shang, K. Wang, F. Liu, Y. Wang, Q. Wang, T. Lu, Z.-K. Liu, Phase stability, elastic, and thermodynamic properties of the L1 $_2$ (Co,Ni) $_3$ (Al,Mo,Nb) phase from first-principles calculations, J. Mater. Res. 32 (2017) 2100–2108, https://doi.org/10.1557/jmr.2017.8.

[30] P. Pandey, S.K. Makineni, A. Samanta, A. Sharma, S.M. Das, B. Nithin, C. Srivastava, A.K. Singh, D. Raabe, B. Gault, K. Chattopadhyay, Elemental site occupancy in the L12 A3B ordered intermetallic phase in Co-based superalloys and its influence on the microstructure, Acta Mater. (2018), https://doi.org/10.1016/j.actamat.2018.09.049.

[31] A. Tomaszewska, T. Mikuszewski, G. Moskal, D. Migas, Primary microstructure, microsegregation and precipitates characterization of an as-cast new type γ-γ′ Co-Al-Mo-Nb cobalt-based superalloy, J. Alloys Compd. 750 (2018) 741–749, https://doi.org/10.1016/j.jallcom.2018.03.397.

[32] Q. Liu, J. Coakley, D.N. Seidman, D.C. Dunand, Precipitate evolution and creep behavior of a W-free Co-based superalloy, Metall. Mater. Trans. A Phys. Metall. Mater. Sci. 47 (2016) 6090–6096, https://doi.org/10.1007/s11661-016-3775-1.

[33] L. Wang, M. Oehring, Y. Liu, U. Lorenz, F. Pyczak, Site occupancy of alloying elements in the L12 structure determined by channeling enhanced microanalysis in γ/γ' Co-9Al-9W-2X alloys, Acta Mater. 162 (2019) 176–188, https://doi.org/10.1016/j.actamat.2018.09.059.

[34] I. Povstugar, P.P. Choi, S. Neumeier, A. Bauer, C.H. Zenk, M. Göken, D. Raabe, Elemental partitioning and mechanical properties of Ti- and Ta-containing Co-Al-W-base superalloys studied by atom probe tomography and nanoindentation, Acta Mater. 78 (2014) 78–85, https://doi.org/10.1016/j.actamat.2014.06.020.

[35] F. Xue, H.J. Zhou, X.F. Ding, M.L. Wang, Q. Feng, Improved high temperature γ' stability of Co-Al-W-base alloys containing Ti and Ta, Mater. Lett. 112 (2013) 215–218, https://doi.org/10.1016/j.matlet.2013.09.023.

[36] T. Omori, K. Oikawa, J. Sato, I. Ohnuma, U.R. Kattner, R. Kainuma, K. Ishida, Partition behavior of alloying elements and phase transformation temperatures in Co-Al-W-base quaternary systems, Intermetallics 32 (2013) 274–283, https://doi.org/10.1016/j.intermet.2012.07.033.

[37] C.H. Zenk, S. Neumeier, H.J. Stone, M. Göken, Mechanical properties and lattice misfit of γ/γ' strengthened Co-base superalloys in the Co-W-Al-Ti quaternary system, Intermetallics 55 (2014) 28–39, https://doi.org/10.1016/j.intermet.2014.07.006.

[38] K. Shinagawa, T. Omori, J. Sato, K. Oikawa, I. Ohnuma, R. Kainuma, K. Ishida, Phase equilibria and microstructure on γ′ phase in Co-Ni-Al-W system, Mater. Trans. 49 (2008) 1474–1479, https://doi.org/10.2320/matertrans.mer2008073.

[39] D.J. Sauza, D.C. Dunand, R.D. Noebe, D.N. Seidman, γ'-(L12) precipitate evolution during isothermal aging of a CoAlWNi superalloy, Acta Mater. 164 (2019) 654–662, https://doi.org/10.1016/J.ACTAMAT.2018.11.014.

[40] S. Meher, H.Y. Yan, S. Nag, D. Dye, R. Banerjee, Solute partitioning and site preference in γ/γ' cobalt-base alloys, Scripta Mater. 67 (2012) 850–853, https://doi.org/10.1016/j.scriptamat.2012.08.006.

[41] L. Klein, Y. Shen, M.S. Killian, S. Virtanen, Effect of B and Cr on the high temperature oxidation behaviour of novel γ/γ'-strengthened Co-base superalloys, Corros. Sci. 53 (2011) 2713–2720, https://doi.org/10.1016/J.CORSCI.2011.04.020.

[42] M. Weiser, M.C. Galetz, H.-E. Zschau, C.H. Zenk, S. Neumeier, M. Göken, S. Virtanen, Influence of Co to Ni ratio in γ′-strengthened model alloys on oxidation resistance and the efficacy of the halogen effect at 900 °C, Corros. Sci. 156 (2019) 84–95, https://doi.org/10.1016/J.CORSCI.2019.05.007.

[43] H.-Y. Yan, V.A. Vorontsov, D. Dye, Effect of alloying on the oxidation behaviour of Co–Al–W superalloys, Corros. Sci. 83 (2014) 382–395, https://doi.org/10.1016/J.CORSCI.2014.03.002.

[44] P.J. Bocchini, C.K. Sudbrack, R.D. Noebe, D.C. Dunand, D.N. Seidman, Microstructural and creep properties of boron- and zirconium-containing cobalt-based superalloys, Mater. Sci. Eng. A 682 (2017) 260–269, https://doi.org/10.1016/j.msea.2016.10.124.

[45] M. Kolb, L.P. Freund, F. Fischer, I. Povstugar, S.K. Makineni, B. Gault, D. Raabe, J. Müller, E. Spiecker, S. Neumeier, M. Göken, On the grain boundary strengthening effect of boron in γ/γ′ Cobalt-base superalloys, Acta Mater. 145 (2018) 247–254, https://doi.org/10.1016/j.actamat.2017.12.020.

[46] C.P. Wang, S. Yang, S.Y. Yang, D. Wang, J.J. Ruan, J. Li, X.J. Liu, Experimental investigation of the phase equilibria in the Co-Nb-V ternary system, J. Phase Equilibria Diffus. 36 (2015) 592–598, https://doi.org/10.1007/s11669-015-0407-1.

[47] A. Suzuki, H. Inui, T.M. Pollock, L12 - strengthened cobalt-base superalloys, Annu. Rev. Mater. Res. 45 (2015) 345–368, https://doi.org/10.1146/annurev-matsci-070214-021043.

[48] S. Qu, Y. Li, M. He, C. Wang, X. Liu, Y. Chen, Y. Yang, Microstructural evolution and compression property of a novel γ′-strengthened directionally solidified CoNi-base superalloy, Mater. Sci. Eng. A 761 (2019) 138034, https://doi.org/10.1016/J.MSEA.2019.138034.

[49] P. Viatour, J.M. Drapier, D. Coutsouradis, Stability of the gamma prime -Co3Ti compound in simple and complex Co alloys, Cobalt (1973) 67–74.

[50] X. Liu, Y. Pan, Y. Chen, J. Han, S. Yang, J. Ruan, C. Wang, Y. Yang, Y. Li, X. Liu, Y. Pan, Y. Chen, J. Han, S. Yang, J. Ruan, C. Wang, Y. Yang, Y. Li, Effects of Nb and W additions on the microstructures and mechanical properties of novel γ/γ' Co-V-Ti-based superalloys, Metals (Basel) 8 (2018) 563, https://doi.org/10.3390/met8070563.

[51] B. Yoo, H.J. Im, J.-B. Seol, P.-P. Choi, On the microstructural evolution and partitioning behavior of L12-structured γ′-based Co-Ti-W alloys upon Cr and Al alloying, Intermetallics 104 (2019) 97–102, https://doi.org/10.1016/J.INTERMET.2018.10.027.

[52] M. Jiang, G. Saren, S.Y. Yang, H.X. Li, S.M. Hao, Phase equilibria in Co-rich region of Co-Ti-Ta system, Trans. Nonferrous Met. Soc. China (English Ed.) 21 (2011) 2391–2395, https://doi.org/10.1016/S1003-6326(11)61025-X.

[53] G. Cacciamani, R. Ferro, I. Ansara, N. Dupin, Thermodynamic modelling of the Co–Ti system, Intermetallics 8 (2000) 213–222, https://doi.org/10.1016/S0966-9795(99)00098-9.

[54] H.Y. Yan, V.A. Vorontsov, D. Dye, Alloying effects in polycrystalline γ′ strengthened Co-Al-W base alloys, Intermetallics 48 (2014) 44–53, https://doi.org/10.1016/j.intermet.2013.10.022.

[55] C.J. Kuehmann, P.W. Voorhees, Ostwald ripening in ternary alloys, Metall. Mater. Trans. A Phys. Metall. Mater. Sci. 27 (1996) 937–943, https://doi.org/10.1007/bf02649761.

[56] T. Philippe, P.W. Voorhees, Ostwald ripening in multicomponent alloys, Acta Mater. 61 (2013) 4237–4244, https://doi.org/10.1016/j.actamat.2013.03.049.

[57] M.S. Atas, M. Yildirim, Temporal evolution, coarsening behavior and oxidation resistance of Ni–15Al superalloy, J. Alloys Compd. 809 (2019) 151784, https://doi.org/10.1016/J.JALLCOM.2019.151784.

[58] A.J. Ardell, The effects of elastic interactions on precipitate microstructural evolution in elastically inhomogeneous nickel-base alloys, Philos. Mag. 94 (2014) 2101–2130, https://doi.org/10.1080/14786435.2014.906756.

[59] M. Cottura, Y. Le Bouar, B. Appolaire, A. Finel, Role of elastic inhomogeneity in the development of cuboidal microstructures in Ni-based superalloys, Acta Mater. 94 (2015) 15–25, https://doi.org/10.1016/J.ACTAMAT.2015.04.034.

[60] C. Sagui, D. Orlikowski, A.M. Somoza, C. Roland, Three-dimensional simulations of Ostwald ripening with elastic effects, Phys. Rev. E. 58 (1998) R4092–R4095, https://doi.org/10.1103/PhysRevE.58.R4092.

[61] M. Kolb, C.H. Zenk, A. Kirzinger, I. Povstugar, D. Raabe, S. Neumeier, M. Göken, Influence of rhenium on γ′-strengthened cobalt-base superalloys, J. Mater. Res. 32 (2017) 2551–2559, https://doi.org/10.1557/jmr.2017.242.

[62] I. Povstugar, C.H. Zenk, R. Li, P.-P. Choi, S. Neumeier, O. Dolotko, M. Hoelzel, M. Göken, D. Raabe, Elemental partitioning, lattice misfit and creep behaviour of Cr containing γ ′ strengthened Co base superalloys, Mater. Sci. Technol. 32 (2016) 220–225, https://doi.org/10.1179/1743284715y.0000000112.

[63] S. Meher, L.J.J. Carroll, T.M.M. Pollock, M.C.C. Carroll, Solute partitioning in multi-component γ/γ′ Co-Ni-base superalloys with near-zero lattice misfit, Scripta Mater. 113 (2016) 185–189, https://doi.org/10.1016/j.scriptamat.2015.10.039.
[64] P.J. Bocchini, C.K. Sudbrack, R.D. Noebe, D.N. Seidman, Temporal evolution of a model Co-Al-W superalloy aged at 650 °C and 750 °C, Acta Mater. 159 (2018) 197–208, https://doi.org/10.1016/j.actamat.2018.08.014.
[65] F.R.N. Nabarro, H.L. Villiers, The Physics of Creep, 1995.
[66] M.E. Kassner, M.T. Pérez-Prado, Fundamentals of Creep in Metals and Alloys, Elsevier Ltd, 2004, https://doi.org/10.1016/B978-0-08-043637-1.X5000-5.
[67] A. Bauer, S. Neumeier, F. Pyczak, R.F. Singer, M. Göken, Creep properties of different γ'-strengthened Co-base superalloys, Mater. Sci. Eng. A 550 (2012) 333–341, https://doi.org/10.1016/j.msea.2012.04.083.
[68] A. Bauer, S. Neumeier, F. Pyczak, M. Göken, Creep strength and microstructure of polycrystalline γ′ - strengthened cobalt-base superalloys, Superalloys 2012 (2012) 695–703, https://doi.org/10.1002/9781118516430.ch77.
[69] D.-W. Chung, J. Perrin Toinin, E.A. Lass, D.N. Seidman, D.C. Dunand, Effects of Cr on the properties of multicomponent cobalt-based superalloys with ultra high γ' volume fraction, J. Alloys Compd. 832 (2020) 154790, https://doi.org/10.1016/j.jallcom.2020.154790.
[70] D.S. Ng, D.-W. Chung, J. Perrin Toinin, E.A. Lass, D.N. Seidman, D.C. Dunand, Effect of Cr additions on a γ-γ' microstructure and creep behavior of a Co-based superalloy with low W content, Mater. Sci. Eng. A 778 (2020) 139108, https://doi.org/10.1016/j.msea.2020.139108.
[71] Y. Li, F. Pyczak, J. Paul, M. Oehring, U. Lorenz, Z. Yao, Y. Ning, Rafting of γ′ precipitates in a Co-9Al-9W superalloy during compressive creep, Mater. Sci. Eng. A 719 (2018) 43–48, https://doi.org/10.1016/j.msea.2018.02.017.
[72] F. Pyczak, A. Bauer, M. Göken, S. Neumeier, U. Lorenz, M. Oehring, N. Schell, A. Schreyer, A. Stark, F. Symanzik, Plastic deformation mechanisms in a crept L1 2 hardened Co-base superalloy, Mater. Sci. Eng. A 571 (2013) 13–18, https://doi.org/10.1016/j.msea.2013.02.007.
[73] Y. Li, F. Pyczak, J. Paul, M. Oehring, U. Lorenz, Z. Yao, Microstructure evolution in L12 hardened Co-base superalloys during creep, J. Mater. Res. 32 (2017) 4522–4530, https://doi.org/10.1557/jmr.2017.362.
[74] F.B. Ismail, V.A. Vorontsov, T.C. Lindley, M.C. Hardy, D. Dye, B.A. Shollock, Alloying effects on oxidation mechanisms in polycrystalline Co–Ni base superalloys, Corros. Sci. 116 (2017) 44–52, https://doi.org/10.1016/J.CORSCI.2016.12.009.
[75] F.-C. Kong, Y.-F. Li, C. Shang, Z.-P. Liu, Stability and phase transition of cobalt oxide phases by machine learning global potential energy surface, J. Phys. Chem. C 123 (2019) 17539–17547, https://doi.org/10.1021/acs.jpcc.9b02842.
[76] Q. Wang, Q. Yao, Y. Wang, Y.-H. Zhu, T. Lu, Research on the oxidation behavior of novel γ/γ′-strengthened Co–9Al–10W alloys combined with chromium and rare earth elements, J. Mater. Res. 31 (2016) 3332–3344, https://doi.org/10.1557/jmr.2016.345.
[77] S.M. Das, M.P. Singh, K. Chattopadhyay, Evolution of oxides and their microstructures at 800°C in a γ-γ' stabilised Co-Ni-Al-Mo-Ta superalloy, Corros. Sci. 155 (2019) 46–54, https://doi.org/10.1016/J.CORSCI.2019.02.013.
[78] L. Klein, A. Zendegani, M. Palumbo, S.G. Fries, S. Virtanen, First approach for thermodynamic modelling of the high temperature oxidation behaviour of ternary γ′-strengthened Co–Al–W superalloys, Corros. Sci. 89 (2014) 1–5, https://doi.org/10.1016/J.CORSCI.2014.08.016.
[79] L. Klein, S. Virtanen, Electrochemical characterisation of novel γ/γ′-strengthened Co-base superalloys, Electrochim. Acta 76 (2012) 275–281, https://doi.org/10.1016/J.ELECTACTA.2012.05.016.
[80] Y. Li, F. Pyczak, J. Paul, Z. Yao, Oxidation behaviors of Co-Al-W-0.1B superalloys in a long-term isothermal exposure at 900 °C, J. Mater. Sci. Technol. 34 (2018) 2212–2217, https://doi.org/10.1016/J.JMST.2018.03.013.
[81] L. Klein, M.S. Killian, S. Virtanen, The effect of nickel and silicon addition on some oxidation properties of novel Co-based high temperature alloys, Corros. Sci. 69 (2013) 43–49, https://doi.org/10.1016/J.CORSCI.2012.09.046.
[82] L. Klein, A. Bauer, S. Neumeier, M. Göken, S. Virtanen, High temperature oxidation of γ/γ′-strengthened Co-base superalloys, Corros. Sci. 53 (2011) 2027–2034, https://doi.org/10.1016/J.CORSCI.2011.02.033.
[83] N. Birks, G.H. Meier, F.S. Pettit, Introduction to the High Temperature Oxidation of Metals, second ed., 2006, https://doi.org/10.1017/CBO9781139163903.
[84] Physical ceramics: principles for ceramic science and engineering, Choice Rev. (1996), https://doi.org/10.5860/choice.34-1566. Online.
[85] S. Cruchley, H.E. Evans, M.P. Taylor, M.C. Hardy, S. Stekovic, Chromia layer growth on a Ni-based superalloy: sub-parabolic kinetics and the role of titanium, Corros. Sci. 75 (2013) 58–66, https://doi.org/10.1016/J.CORSCI.2013.05.016.
[86] B. Chattopadhyay, G.C. Wood, The transient oxidation of alloys, Oxid. Metals 2 (1970) 373–399, https://doi.org/10.1007/BF00604477.
[87] C.H. Zenk, S. Neumeier, N.M. Engl, S.G. Fries, O. Dolotko, M. Weiser, S. Virtanen, M. Göken, Intermediate Co/Ni-base model superalloys — thermophysical properties, creep and oxidation, Scripta Mater. 112 (2016) 83–86, https://doi.org/10.1016/J.SCRIPTAMAT.2015.09.018.
[88] S. Kamal, R. Jayaganthan, S. Prakash, S. Kumar, Hot corrosion behavior of detonation gun sprayed Cr3C2–NiCr coatings on Ni and Fe-based superalloys in Na2SO4–60% V2O5 environment at 900 °C, J. Alloys Compd. 463 (2008) 358–372, https://doi.org/10.1016/J.JALLCOM.2007.09.019.